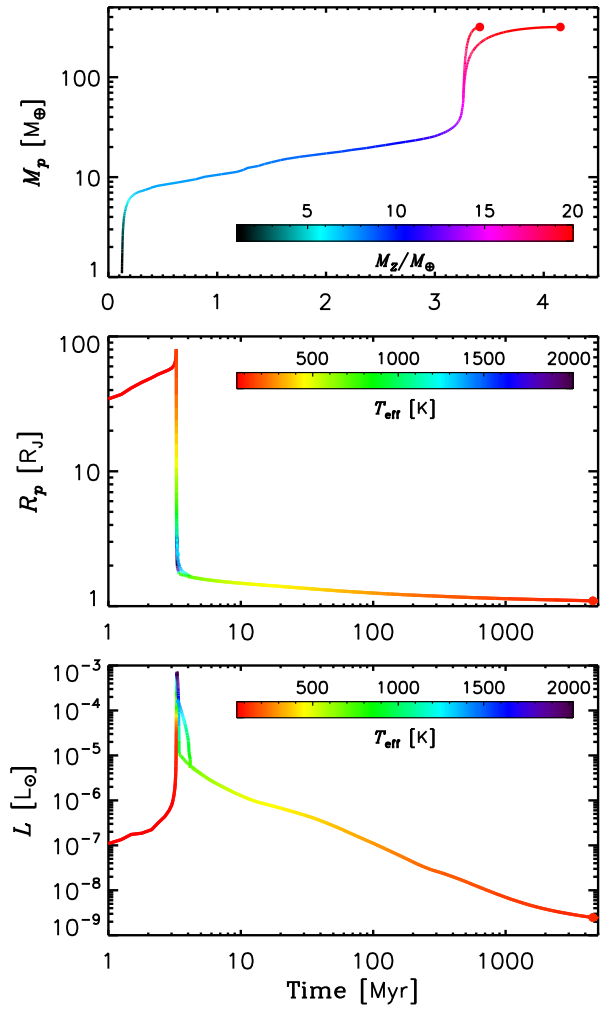


Graphical Abstract

Growth of Jupiter: Formation in Disks of Gas and Solids and Evolution to the Present Epoch

Gennaro D'Angelo, Stuart J. Weidenschilling, Jack J. Lissauer, Peter Bodenheimer



Highlights

Growth of Jupiter: Formation in Disks of Gas and Solids and Evolution to the Present Epoch

Gennaro D'Angelo, Stuart J. Weidenschilling, Jack J. Lissauer, Peter Bodenheimer

- Jupiter's formation is modeled via core-nucleated accretion
- Solids' accretion accounts for interactions with an evolving disk of planetesimals
- Evolution within a dispersing nebula is approximated via simplified disk models
- Structure calculations are performed throughout the planet's history, for 5 Gyr
- Final radii and luminosities agree with those of Jupiter within 10%

Growth of Jupiter: Formation in Disks of Gas and Solids and Evolution to the Present Epoch^{*}

Gennaro D'Angelo^{a,*}, Stuart J. Weidenschilling^b, Jack J. Lissauer^c and Peter Bodenheimer^d

^aTheoretical Division, Los Alamos National Laboratory, Los Alamos, NM 87545, USA

^bPlanetary Science Institute, 1700 East Fort Lowell Road, Suite 106, Tucson, AZ 85719, USA

^cSpace Science and Astrobiology Division, NASA-Ames Research Center, Moffett Field, CA 94035, USA

^dUCO/Lick Observatory, Department of Astronomy and Astrophysics, University of California, Santa Cruz, CA 95064, USA

ARTICLE INFO

Keywords:

Accretion
Jovian planets
Jupiter
Planetary formation
Planetesimals

Received: 10 Mar 2020

Revised: 22 Aug 2020

Accepted: 25 Aug 2020

This is an unofficial preprint prepared
by the authors.

Abstract

The formation of Jupiter is modeled via core-nucleated accretion, and the planet's evolution is simulated up to the present epoch. Throughout the phases when the planet acquires most of its heavy-element content, the calculation of solids' accretion accounts for interactions with an evolving disk of planetesimals. The phase of growth from an embryo of a few hundred kilometers in radius until the time when the accretion of gas overtakes solids' accretion was presented by D'Angelo et al. (2014), and the same numerical methods are applied here. Those calculations followed the formation for about 4×10^5 years, until the epoch when the heavy-element and hydrogen/helium masses were $M_Z \approx 7.3$ and $M_{XY} \approx 0.15$ Earth's masses (M_\oplus), respectively, and $\dot{M}_{XY} \approx \dot{M}_Z$. Herein, the calculation is continued through the phase when M_{XY} grows to equal M_Z , at which age, about 2.4×10^6 years, the total mass of the planet is $M_p \approx 20 M_\oplus$. About 9×10^5 years later, M_p is approximately $60 M_\oplus$ and $M_Z \approx 16 M_\oplus$, three-quarters of which are delivered by planetesimals larger than 10 km in radius. Around this epoch, the contraction of the envelope dictates gas accretion rates a few times $10^{-3} M_\oplus$ per year, initiating the regime of disk-limited accretion, whereby the planet can accrete all the gas provided by the disk, and its evolution is therefore tied to disk's evolution. Growth is continued by constructing simplified models of protosolar accretion disks that evolve through viscous diffusion, winds, and accretion on the planet. Jupiter's formation ends after $\approx 3.4\text{--}4.2$ Myr, depending on the applied disk viscosity parameter, when nebula gas disperses. The young Jupiter is 4.5–5.5 times as voluminous as it is presently and thousands of times as luminous, $\sim 10^{-5} L_\odot$. The heavy-element mass is $\approx 20 M_\oplus$. The evolution proceeds through the cooling and contraction phase, in isolation except for solar irradiation. After 4570 Myr, the age of the solar system, radius and luminosity of the planet are within 10% of current values, accounting also for uncertainties in the power absorbed from the Sun. During formation, and soon thereafter, the planet exhibits features, e.g., luminosity and effective temperature, that may probe aspects of the latter stages of formation, if observable. These possibly distinctive features, however, seem to disappear within a few tens of Myr.

^{*}This document is the result of a research project partly funded by NASA.

^{*}Corresponding author

 gennaro@lanl.gov (G. D'Angelo); sjw@psi.edu (S. J. Weidenschilling); Jack.J.Lissauer@nasa.gov (J. J. Lissauer); peter@ucolick.org (P. Bodenheimer)
ORCID(s): 0000-0002-2064-0801 (G. D'Angelo); 0000-0001-6513-1659 (J. J. Lissauer); 0000-0001-6093-3097 (P. Bodenheimer)

1. Introduction

Jupiter is by far the most massive planet in the Solar System, and its large abundances of hydrogen and helium imply that it must have formed rapidly, while a significant amount of gas still remained within the *solar nebula*, the protosolar accretion disk. Although it is not known at what point of the nebula evolution the young Jupiter began to accrete significant amounts of gas, the planet likely acquired most of its H/He content toward the latter stages of the nebula life, before the gas around Jupiter's orbit was ultimately dispersed by thermal and magnetic winds (e.g., Armitage, 2020).

Formation according to core-nucleated accretion (Pollack et al., 1996) requires the assembly of a planet of at least several Earth masses (M_{\oplus}) from the solids originally present in the solar nebula. In fact, only then can the planet start collecting significant amounts of hydrogen and helium. In a scenario in which the core's building blocks are mostly planetesimals of tens of kilometers (or larger) in size, the reservoir of solids is nearly local, radially extending a few to several Hill radii from the planet's orbit (Lissauer, 1987). One requirement to initiate formation is then that the swarm of planetesimals be massive enough to allow for the rapid "monarchical" growth of a seed body (Weidenschilling, 2005), the planetary embryo. In this case, the growth of the embryo, which becomes the planet's core, can proceed until the swarm around its orbit is severely depleted.

Modeling the initial evolution of the embryo of a gas giant, and the subsequent accretion of solids, is challenging in several aspects (e.g., Chambers et al., 2010, and references therein). Previous models of Jupiter's formation used simplified methods for computing the accretion of heavy elements, based primarily on semi-analytical approximations (e.g., Lissauer et al., 2009; Mordasini et al., 2012, and references therein). In D'Angelo et al. (2014, henceforth referred to as Paper I), we modeled the early stages of Jupiter's growth applying a numerical/statistical approach to calculate the accretion of solids, starting from a 350 km radius planetesimal evolving in an active swarm of solid bodies tens of meters to hundreds of kilometers in size. A number of effects were included to mimic the evolution and interactions of the bodies within the swarm, although we neglected any possible radial migration of the planet due to interactions with the swarm and the surrounding gas (e.g., Nelson, 2018, and references therein).

Paper I modeled the rapid growth of the planet's core, up to $\approx 7.3 M_{\oplus}$, until the accretion rates of gas and solids were approximately equal. At that point of the evolution, only 2 percent of the planet's mass was in hydrogen and helium. Results indicated that planetesimals larger than 10 km in radius still provided the bulk of the planet's heavy-element content and that the voluminous – but initially very low-density gaseous envelope – substantially increased the rate of accretion of solids for planet masses as small as $\approx 1 M_{\oplus}$.

We extend herein the simulation of the growth of Jupiter presented in Paper I, from about 4×10^5 years until the planet reaches one Jupiter mass, and then evolve it forward in the presence of solar radiation until the present epoch. The

numerical methods are described in Section 2. Section 3 presents the results of our simulations. We summarize the results and discuss their implications in Section 4. Our results are compared with those from some previous formation studies (Movshovitz et al., 2010; Alibert et al., 2018; Shibata and Ikoma, 2019) in Section 4 and with post-formation calculations (Burrows et al., 1997; Baraffe et al., 2003, 2008) and measurements of Jupiter's atmosphere (Seiff et al., 1998) in Appendix A, where the effects of some model assumptions are also discussed.

2. Numerical Methods

The structure and evolution of the planet is calculated according to the methods described in Paper I. In that study, we investigated the initial assembly of Jupiter at 5.2 au from the Sun, in a nebula with a local surface density of solids of initial value $\sigma_Z^0 = 10 \text{ g cm}^{-2}$ (see Equation (2)), starting from a planetary embryo of 350 km in radius ($\approx 10^{-4} M_{\oplus}$). The evolution was calculated for $\approx 4 \times 10^5$ years, at which point the accretion rate of gas had surpassed that of solids. At the epoch when the two accretion rates were approximately equal, $\approx 3 \times 10^{-6} M_{\oplus} \text{ yr}^{-1}$, the mass in heavy elements was $7.3 M_{\oplus}$ and that of hydrogen and helium gas was $\approx 0.15 M_{\oplus}$.

In the remainder of this section we briefly describe the main components of the model used to simulate the formation up to Jupiter's mass, and calculate the subsequent evolution of the planet up to an age of $\approx 5 \times 10^9$ years. We indicate with M_Z the mass of heavy elements and with M_{XY} the hydrogen/helium mass of the planet. Heavy elements are supplied by accretion of planetesimals, here assumed to be solid bodies larger than 30 m in diameter. The total mass of the planet is $M_p = M_Z + M_{XY}$. In these calculations, for compositional purposes, there is no dissolution of heavy elements, which are assumed to rain out onto a central (condensed) core.

2.1. Structure Calculations

The interior structure of the planet consists of an inner condensed heavy-element ($Z > 2$) core and an exterior envelope of hydrogen and helium. The condensed core is assumed to be incompressible, i.e.,

$$\frac{dR_Z}{dM_Z} = \frac{1}{4\pi\rho_Z R_Z^2}, \quad (1)$$

where R_Z is the core radius and ρ_Z , the core density, is a constant. The effects of this approximation are evaluated in Appendix A through core structure calculations, by applying temperature and pressure at the core-envelope boundary as M_Z and M_{XY} grow.

The envelope structure is computed by applying the standard equations of stellar structure (e.g., Weiss et al., 2006; Kippenhahn et al., 2013), in which the gravitational energy released by incoming (i.e., accreted) solids represents a depth-dependent energy source. These equations are solved as described in, e.g., Pollack et al. (1996), Bodenheimer et al. (2000), and Hubickyj et al. (2005), with the modification detailed in Paper I. The composition of the envelope gas is

assumed to have a near-protosolar (see Asplund et al., 2009) mass ratio of hydrogen and helium (mass fractions $X = 0.74$ and $Y = 0.24$, respectively), with a small admixture of heavier elements.

The structure equations are integrated from the inner boundary of the envelope, R_Z (which varies according to Equation (1)), out to the planet radius R_p . In these models R_p is approximated by an effective radius R_{eff} (also referred to as “accretion” radius), where $1/R_{\text{eff}} \geq 1/R_B + k/R_H$, in which R_B and R_H are the Bondi and Hill radius of the planet, respectively. When the equality holds, which occurs for most of the planet formation history, the planet is *in contact* with the surrounding nebula and the density and temperature at R_p are those of the nebula gas. During later stages of formation, when the planet gains most of its mass, it contracts rapidly and detaches from the nebula. The envelope’s boundary conditions for these stages are discussed in Bodenheimer et al. (2000) and D’Angelo and Bodenheimer (2016). For $M_p/M_\odot \ll 1$, the quantity k above has a theoretical lower bound of $k \approx 1.415$ (set by the volumetric mean-radius of the planet’s Roche lobe, Eggleton, 1983), which would be applicable in the limit of an inviscid and pressureless nebula gas. This quantity is expected to be an increasing function of the nebula kinematic viscosity and pressure scale-height. For typical nebula conditions at Jupiter’s location, it was determined through high-resolution three-dimensional hydrodynamic simulations that $k \approx 4$ (Lissauer et al., 2009). For a given gas viscosity, k is expected to decrease at smaller heliocentric distances (Bodenheimer et al., 2018). Since $R_B \propto M_p$ and $R_H \propto M_p^{1/3}$, the planet radius is more likely governed by the Bondi radius at low planet masses and by the Hill radius at later evolutionary stages (D’Angelo and Bodenheimer, 2013), before the planet starts the phase of rapid contraction (see Section 3.2). Nebula-planet tidal interactions, quantified on average by the factor k , can potentially modify this connection so that $R_{\text{eff}} \approx R_H/k$ even at relatively early stages of evolution. Moreover, since R_B is also inversely proportional to the nebula temperature, the radius of a planet may become more closely tied to R_H/k as the nebula ages and cools down, especially for planets orbiting close to their star.

The calculation of the envelope structure includes the computation of *a*) the trajectories and the ablation rates of the solids moving through the envelope (Podolak et al., 1988; Pollack et al., 1996); *b*) the opacity of dust grains released in the envelope by ablating solids, taking into account the coagulation and settling of the particles (Movshovitz et al., 2010); and *c*) the accretion of nebular gas, including limiting accretion rates dictated by disk-planet tidal interactions (Lissauer et al., 2009; Bodenheimer et al., 2013).

The calculation of the interactions between incoming solids and envelope gas also provides the effective cross-section of the planet for the capture of planetesimals, as a function of the planetesimal radius (see details in Paper I). Once in the envelope, solids are tracked until they break up, are completely consumed by ablation, or reach the core. As solids travel through the envelope, they shed mass and release

energy. The energy released at a given depth contributes to the energy budget of that envelope layer. The mass deposited by ablation provides the input for the dust opacity calculation. This mass, however, is assumed to sink to the bottom of the envelope and adds to the mass of the core. The effects of height-dependent dissolution of heavy elements in the envelope, such as those considered by Bodenheimer et al. (2018), are not included in these calculations. Jupiter formation models that account for the atmospheric deposition of heavy elements (via ablation and break-up) will be presented elsewhere.

2.2. Accretion of solids

The numerical methods employed to simulate the evolution of a disk of planetesimals are described in Weidenschilling et al. (1997) and Weidenschilling (2011). The code computes collisional and gravitational interactions within a swarm of planetesimals that extends over a radial distance of several to many Hill radii on either side of the embryo’s or planet’s orbit. The swarm is divided into a number of radial zones. Both the number and width of the radial zones vary as the core grows (e.g., see details in the caption of Figure 1). In each zone, solids are distributed within a series of size bins so that the mean planetesimal mass in two adjacent bins differs by a factor of two (i.e., a factor of ≈ 1.26 difference in radius). Each bin is also characterized by mean values of orbital eccentricity and inclination, which evolve due to viscous stirring, dynamical friction, and gas drag. The effects of gas drag on planetesimal orbits are implemented according to the formulations of Adachi et al. (1976), Weidenschilling (1977), and Kary et al. (1993). The evolution of solids also includes the process of shepherding, as discussed in Paper I (and references therein), and gravitational scattering due to close encounters inside $\approx R_H$ of the growing planet.

The orbital elements of the bodies are used to detect intersecting orbits and to compute impact probabilities. Collisions may result in erosion, fragmentation or merging, which cause the size distribution of the solids within each zone to evolve over time and transfer mass between radial zones (when orbits are sufficiently altered by collisions, see details in Weidenschilling et al., 1997). Since the planetesimals’ dynamics is assumed to be Keplerian and gas drag dominates the orbital evolution of small solids, bodies smaller than ≈ 15 m in radius are removed from the calculation (i.e., by assumption, these small bodies do not further contribute to the evolution of the swarm and the growth of the planet). Capture and concentration of bodies caused by drag forces arising from variations of the radial gradient of the gas pressure in the nebula are not modeled and neither is capture in mean motion resonances (for further discussion, see Kary et al., 1993; Kary and Lissauer, 1995). These calculations also neglect the effects of additional embryos orbiting nearby (see, e.g., Levison et al., 2010).

The planetesimal disk has an initial surface density of solids

$$\sigma_Z^0 = 10 \left(\frac{a_p}{a} \right) \text{ g cm}^{-2}, \quad (2)$$

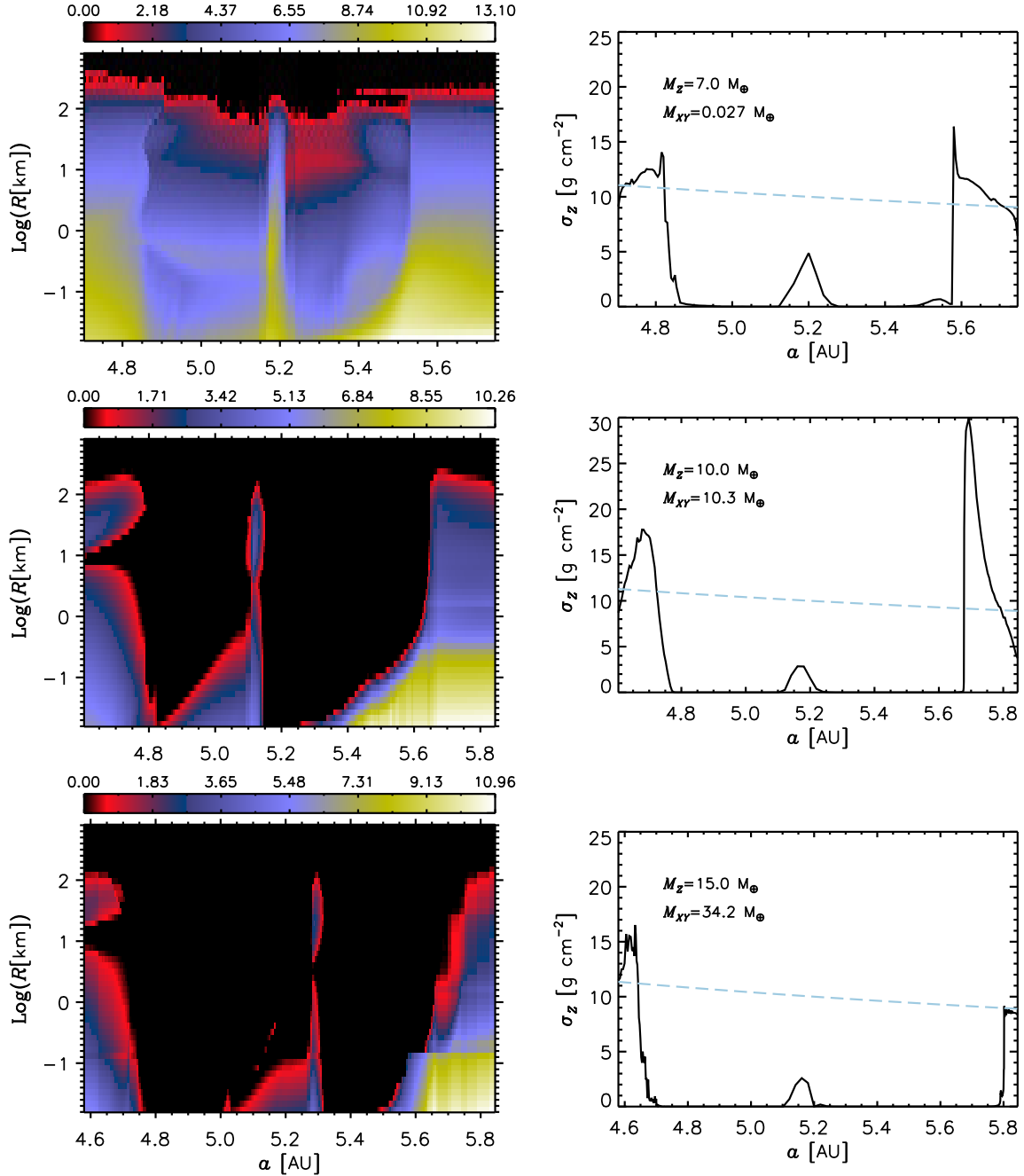


Figure 1: Left: Distributions of planetesimals versus semi-major axis a and radius R . The logarithm of the number of bodies per radial zone and size bin is color-coded at three stages of the planet's growth: $M_Z = 7 M_\oplus$ (top), $10 M_\oplus$, and $15 M_\oplus$ (bottom). The envelope mass is indicated in the right panels. The width of the radial zones varies between 0.0049 and 0.0196 au in the top panel (for a total of 170 zones) and between 0.0003 and 0.02 au in the others (for a total of up to 250 zones). Right: Surface density versus semi-major axis (solid lines) corresponding to the distributions of the left panels. The dashed line represents the initial surface density of solids.

where $a_p = 5.2$ au is the orbital radius of the planet and a is the heliocentric distance of the solids. The initial size distribution is a power law of the planetesimals' radius, $\propto R^{-11/6}$, with R (initially) ranging from ≈ 15 m to 50 km. This slope is characteristic of collisional equilibrium, and while the size distribution is allowed to evolve, the slope remains close to the initial value during the simulations. Accretion tends to

deplete the swarm on both sides of the planet's orbit, over an average radial distance $b R_H$. The depleted region is referred to as the planet's feeding zone for the accretion of solids. In the calculations the value of b is about 3.5 when $M_p \approx 7 M_\oplus$, decreasing to 2.8 when $M_p \approx 49 M_\oplus$ (see Figure 1). At earlier epochs, the region is depleted in solids but not entirely empty (see Paper 1). Gravitational shepherding

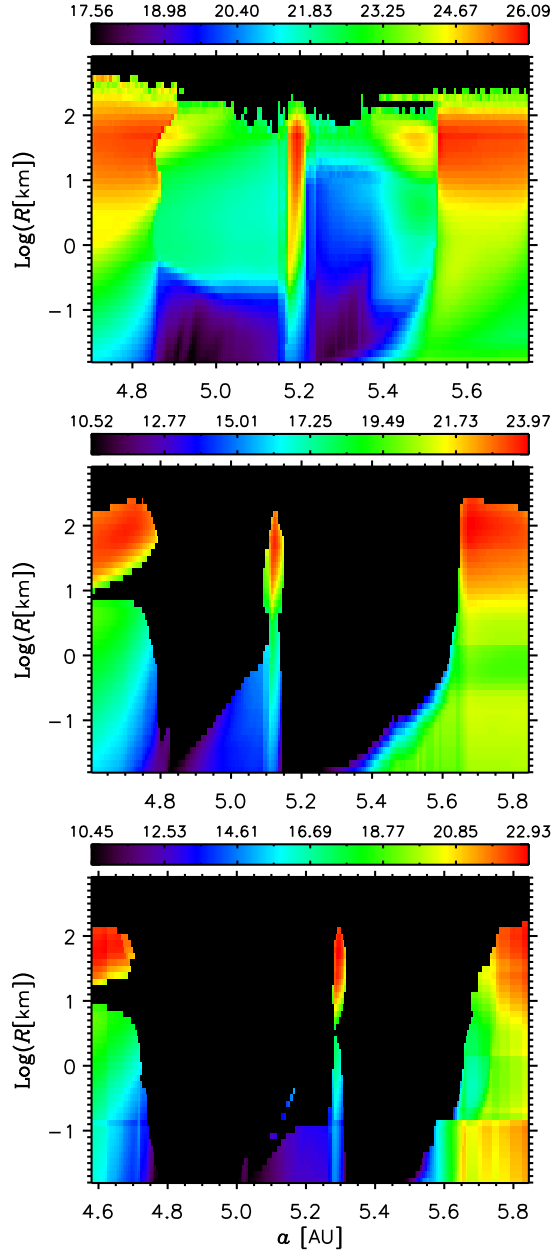


Figure 2: Distributions of the solids' mass versus orbital semi-major axis and planetesimal radius. The logarithm of the mass (in grams) is plotted for each radial zone and size bin at the same epochs as in Figure 1, following the same order from top to bottom.

and gas drag produce a mass pileup at the edges of this region, as illustrated in Figure 1. In order to provide higher spatial resolution near the edges, the zone width is adjusted. This is done by subdividing a zone into two, each with half the width, and the same surface density σ_Z at the moment of division, after which they evolve separately. This procedure is applied sequentially, as required, and allows us to resolve radial features using zones as narrow as needed (< 0.001 au). As a reference, in the calculations the largest zone width at the boundaries between depleted and undepleted regions can be a few percent of R_H , but it is typically much smaller.

Assuming that depletion occurs only via accretion on the planet and that there is no significant re-supply of solids to the region, the heavy-element content of the planet (i.e., the core mass in our case) is determined by the amount of solids initially contained in the region (Lissauer, 1987)

$$M_Z \approx 4\pi b a_p^2 \sigma_Z^0 \left(\frac{M_p}{3M_\odot} \right)^{1/3}, \quad (3)$$

where σ_Z^0 refers to the initial surface density of solids at the planet's orbit, $a = a_p$. When $M_{XY} \ll M_Z$, the mass of heavy elements is proportional to $a_p^3 (b\sigma_Z^0)^{3/2}$ and equal to $\approx 9 M_\oplus$ for $b = 3.5$ (see top panels of Figures 1 and 2). The quantity b is somewhat smaller than the classic value of 4 (Kary and Lissauer, 1994) for the reasons discussed in Paper I. Accounting for solids trapped in Trojan-like orbits, the difference in mass is about 20%. When $M_p \approx 20 M_\oplus$ ($b \approx 3$), Equation (3) predicts $M_Z \approx 10 M_\oplus$, in reasonable accord with the calculation (see Figure 1). In general, and under the assumption of a sufficient reservoir of heavy elements, $M_Z \propto R_H$, i.e., $M_Z \propto M_{XY}^{1/3}$ when $M_{XY} \gg M_Z$. Nonetheless, even if the disk of planetesimals were to extend to infinity, Equation (3) predicts that the incremental gain in heavy elements decreases as the planet mass grows:

$$\frac{dM_Z}{dM_p} \approx \frac{4}{3} b \pi \left(\frac{a_p^2 \sigma_Z^0}{M_p} \right) \left(\frac{M_p}{3M_\odot} \right)^{1/3}. \quad (4)$$

Other effects, such as gravitational scattering and competing depletion by nearby planets or planetary embryos, are likely important and can reduce the supply of solids available for accretion. It should be noted, however, that in the calculations presented here Equation (3) does not strictly apply because of the additive effects of drag forces and interactions among planetesimals.

The simulation was initiated with a seed body of about $10^{-4} M_\oplus$, large enough compared to neighboring planetesimals in the swarm to allow for runaway growth. Within $\approx 2 \times 10^4$ years, its mass grows by over a factor of 10. The gravitational perturbations of this body soon become sufficiently large to stir orbital eccentricities in the surrounding region and prevent runaway growth of potential competitors, the largest of which reach sizes of a few to several hundred km in radius.

The initial growth of the embryo assumes that solids can directly impact its surface. In fact, at ≈ 5 au, the radius of the initial seed is much larger than the Bondi radius (assuming a nebula temperature of ≈ 120 K), and the presence of a tenuous atmosphere (which can increase solids' accretion) is not expected until $R_B \gg R_Z$, when $M_Z \gg 0.01 M_\oplus$. At that point, however, the swarm is still largely undepleted and dM_Z/dt is already relatively large, a few times $10^{-5} M_\oplus \text{ yr}^{-1}$. The envelope structure is modeled starting from $M_Z \approx 1 M_\oplus$.

Ongoing accretion of solids and shepherding effects (see, e.g., Greenberg, 1983) generate a gap in the swarm along the orbit of the planet, as can be seen in Figure 1. The figure

shows the number of bodies for each zone (horizontal axis) and size bin (vertical axis) in the left panels and the surface density of solids versus semi-major axis in the right panels, at different epochs, as indicated by the core and envelope masses in the legends. Examples of the same plots at lower masses, reported in Paper I, indicate that the depletion of solids in the gap region is already significant at $M_p \approx 1 M_\oplus$. As shown in Figure 1, this region becomes severely depleted or virtually empty for $M_p \gtrsim 7 M_\oplus$. Gravitational perturbations by the core and drag forces tend to increase the density of solids around the edges of the gap, especially exterior to the orbit (see right panels), as can be noticed by comparing with the initial distribution (dashed line). Also note that the gap is narrower for smaller-size bodies (left panels). Figure 2 shows the mass distribution of the planetesimals, as a function of orbital radius and planetesimal radius, for the same cases as in Figure 1. The figure indicates that planetesimals of several tens of kilometers in radius typically carry most of the mass in the swarm.

The middle and bottom panels of Figure 2 also show a small reservoir of solids in Trojan-like orbits, most of which are present from the beginning of the evolution, trapped there during the initial runaway growth of the core. These bodies cannot collide with the core and can escape only if the orbital eccentricity increases because of collisions or encounters with bodies other than the core. Gas drag may cause these solids (particularly the small ones) to drift in semi-major axis and allow them to escape. Drag-induced decay of orbits is visible in the middle and bottom panels of the figure, especially for $R < 1$ km. It is unclear whether the bodies in Trojan-like orbits, visible in the figure, may survive much longer after Jupiter's formation; the present-day Trojans were possibly trapped much later (e.g., Morbidelli et al., 2005; Nesvorný et al., 2013; and review by Slyusarev and Belskaya, 2014, and references therein)

At the same epochs as in the two previous figures, Figure 3 shows distribution maps of mean eccentricity (left) and inclination (right) of the solids. The swarm remains relatively flat since stirring mostly occurs in the orbital plane of the planet, hence exciting orbital eccentricity more than orbital inclination (see color bar ranges in Figure 3). This is also the case when the planet has lower mass.

2.3. Accretion of gas

The accretion of gas is dictated by envelope contraction for most of the planet's formation history. During this time, contraction is regulated by cooling, which depends on the ability of the outer envelope to radiate away the gravitational energy released by contraction and accretion of solids. In fact, the accretion of gas is correlated to the accretion of solids until the envelope mass exceeds the core mass (see Section 3). Moreover, the lower the opacity is in the outer envelope gas, the faster contraction may proceed (see, e.g., Hubickyj et al., 2005; Movshovitz et al., 2010, and references therein). Here, the accreted gas is assumed to have solar abundances.

Once $M_{XY} \gtrsim M_Z$ and gravitational contraction starts to dominate the energy generation in the envelope, the con-

traction speeds up and dM_{XY}/dt may grow independently of dM_Z/dt . At this point, the only limit to growth is set by the available supply of nebula gas. When tidal interactions between the planet and the disk are negligible, the sustained (i.e., non-transient) accretion rate on the planet would be limited to the accretion rate through a steady-state accretion disk (Lynden-Bell and Pringle, 1974; Pringle, 1981), which is proportional to the kinematic viscosity, ν , and surface density of the gas, Σ . In young, planet-forming nebulae surrounding solar-mass stars, this rate is likely $\gtrsim 10^{-2} M_\oplus \text{ yr}^{-1}$, although it can be much smaller in old disks. Therefore, during most of the planet's evolution, the rate of supply of gas from the nebula is generally significantly larger than the rate of envelope accretion dictated by contraction. But the situation changes as dM_{XY}/dt grows, the rate of supply by the nebula declines over time, and disk-planet tidal interactions alter the dynamics of the gas flux toward the planet.

Gap formation in a gaseous nebula is a consequence of tidal interactions and occurs (around a planet's orbit) when the tidal torques exerted by the planet's gravity overcome viscous torques exerted by adjacent disk rings (e.g., Ward, 1997; Lubow and Ida, 2010, and references therein). Applied to a solar-mass star, the condition reads

$$\left(\frac{M_p}{M_\odot}\right)^2 \gtrsim 3\pi \left(\frac{\nu}{a_p^2 \Omega}\right) \left(\frac{H}{a_p}\right)^3, \quad (5)$$

where H is the nebula pressure scale-height and Ω the local orbital frequency. In a nebula whose temperature is ≈ 120 K (which determines H) and whose viscosity corresponds to an accretion rate on the star of $\approx 10^{-7} M_\odot \text{ yr}^{-1}$ (e.g., Natta et al., 2006), gap formation requires a planet mass $M_p \gg 10^{-4} M_\odot$, or several to many tens of Earth's masses. The flux of gas toward a planet's feeding zone starts to decline as the gap deepens and widens. The complexity of the accretion flow, which is three-dimensional in nature even at much smaller masses (D'Angelo and Bodenheimer, 2013), does not allow simple estimates. Disk-limited rates have been evaluated through multi-dimensional hydrodynamic calculations (see, e.g., Lissauer et al., 2009; Bodenheimer et al., 2013, and references therein). They rapidly decrease as the planet mass increases and, in general, they are lower for cooler and less viscous disks (see D'Angelo and Lubow, 2008). These rates are applied to our spherically symmetric model; thus, the radiated luminosity from behind the accretion shock (assumed to form where the infalling material hits the surface) is approximately given by $GM_p \dot{M}_{XY}/R_p$, and is close to the total luminosity of the planet.

Therefore, once Jupiter started its phase of rapid growth, its evolution likely became tied to that of the surrounding solar nebula. And since the supply of gas to a Jupiter-mass planet is non-negligible (under a broad range of conditions), Jupiter continued to accrete until the surrounding nebula eventually faded away.

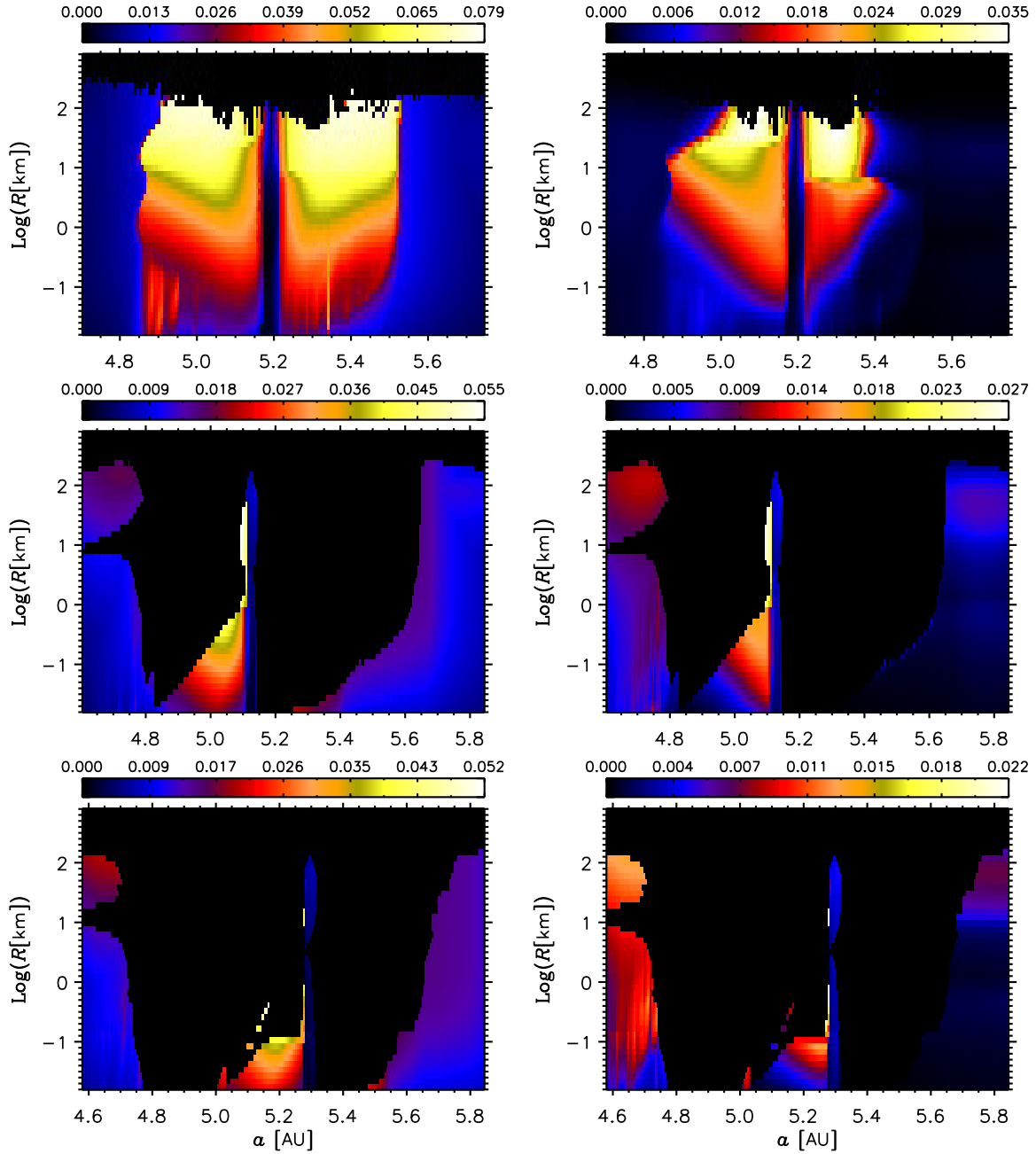


Figure 3: Distributions of the mean orbital eccentricities (left) and of the sine of the mean orbital inclinations (right) of planetesimals as a function of semi-major axis and radius. The distributions are plotted at the same times as in Figure 1, when $M_Z = 7 M_\oplus$ (top), $10 M_\oplus$ ($M_p \approx 20 M_\oplus$), and $15 M_\oplus$ ($M_p \approx 49 M_\oplus$, bottom).

3. Results

Adopting a standard terminology (under the approximations applied here), we denote by “Phase 1” the evolution of the planet up to the time when $dM_{XY}/dt = dM_Z/dt$ and by “Phase 2” the evolution from the end of Phase 1 to the time the crossover mass is attained, $M_{XY} = M_Z$. From then up until the time the surrounding disk dictates the accretion of gas, the evolution is denoted as “Phase 3”.

Previously, we divided Jupiter’s growth into these three phases, based on the results presented in Pollack et al. (1996).

That paper was primarily concerned with the growth of the planet up to the initiation of rapid gas accretion. Our prescriptions for \dot{M}_{XY} beyond that point were physically-motivated in a qualitative sense, but the quantitative implementation was *ad hoc*. But starting with Lissauer et al. (2009), more physics has been used to model the later stages of gas accretion. The transition from cooling-limited accretion to disk-limited accretion is now calculated, and indeed it is more fundamental than our boundaries between Phases 1, 2, and 3. Therefore, to recognize disk-limited accretion as a separate stage of growth, in this paper and henceforth we will refer to the epoch from

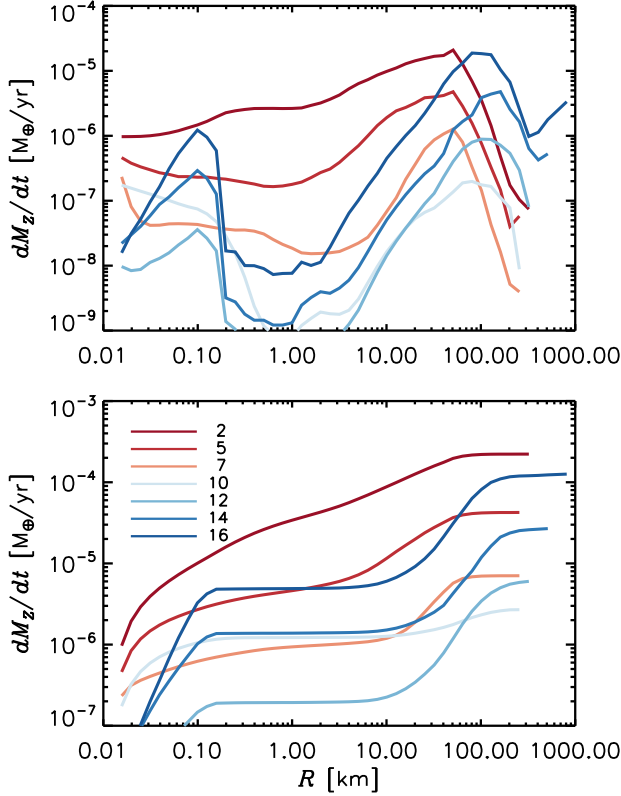


Figure 4: The top panel shows the accretion rate of planetesimals as a function of their radius, R , for different core masses, M_Z , as indicated in the bottom panel in units of M_\oplus . The bottom panel shows the cumulative distributions of the accretion rates, obtained by integrating the distributions of the top panel. The corresponding gas accretion rates are illustrated in Figure 6.

the onset of disk supply-limited gas accretion until the end of gas accretion as “Phase 4”.

Typically, the growth rate of the planet \dot{M}_p/M_p , over its entire history, is largest at the end of Phase 3 and is controlled by the envelope’s contraction rate. The transition to Phase 4 depends on disk properties and planet mass. In this phase, the growth rate becomes tied to the evolution of the surrounding disk, and it slows down as the disk evolves; \dot{M}_{XY} is also determined by tidal interactions between the disk and the planet.

As anticipated above, since a giant planet may grow as long as there is nebula gas near its orbit, the end of Phase 4 typically corresponds with the dispersal of the gas from the planet’s surroundings. After that time, the planet evolves in *isolation*. The inventory of H/He does not change during the evolution in isolation (if there is no or negligible loss by solar irradiation), although the inventory of heavy elements might, due to further collisions with solid bodies.

3.1. Phases 1 and 2

The evolution of the planet during Phase 1 is described in detail in Paper I. The evolution begins at $M_Z \approx 10^{-4} M_\oplus$

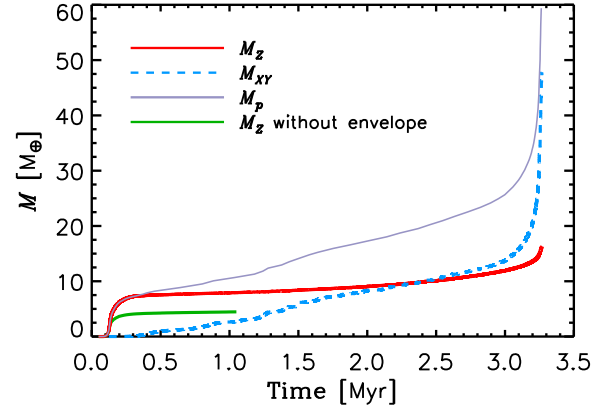


Figure 5: Heavy-element mass, M_Z , and envelope mass, M_{XY} , versus time, as indicated in the legend. The green line represents the bare-core model discussed in D’Angelo et al. (2014). Core and envelope mass are equal at $t \approx 2.38$ Myr, $M_Z = M_{XY} = 9.8 M_\oplus$.

although the structure calculation of the envelope begins at $M_Z \approx 1 M_\oplus$. The growth of the core is initially rapid and proceeds in a runaway fashion, with dM_Z/dt increasing as M_Z increases. During Phase 1, the solids accretion rate reaches a maximum of $2.2 \times 10^{-4} M_\oplus \text{ yr}^{-1}$ at $M_Z \approx 2.1 M_\oplus$ ($M_{XY} \ll M_Z$ at this point). As the swarm around the planet’s orbit depletes, dM_Z/dt begins to decline. The gaseous envelope, although small in mass, is large in volume and significantly increases the capture radius of the planet (which is a function of R) for the accretion of planetesimals, first of small ones (a few to several kilometers in radius) and of all sizes once $M_Z \gtrsim 4 M_\oplus$ ($M_{XY} \gtrsim 10^{-3} M_\oplus$).

The top panel of Figure 4 shows the distribution of dM_Z/dt , versus the planetesimal radius R , for different values of M_Z . The cumulative distributions, obtained by integrating over R the curves in the top panel, are plotted in the bottom panel for the core masses indicated in the legend in units of M_\oplus . During Phase 1, dM_Z/dt is maximum for $R \approx 50$ km bodies and accretion of large planetesimals accounts for most of the heavy-element content of the planet. In fact, by the time $M_Z \approx 7 M_\oplus$, about 70% of the heavy element mass has been delivered by planetesimals $\gtrsim 10$ km in radius and only about 13% by bodies smaller than 1 km in radius.

The accretion rate of solids decreases by a factor of more than 30 as the planet mass grows from $\approx 2 M_\oplus$ to $\approx 7 M_\oplus$. Meanwhile, the accretion rate of gas increases by a similar factor. Although the mass fraction of H/He is still quite small at this time, one percent when $M_p \approx 7.3 M_\oplus$ ($M_{XY} \approx 0.08 M_\oplus$, see Figure 5), the importance of the envelope can be appreciated by comparing M_Z with the case in which a bare core grows in the same swarm, attaining a mass just above $4 M_\oplus$ in 10^6 years, when its accretion rate has dropped to a few times $10^{-7} M_\oplus \text{ yr}^{-1}$ (compare red and green curves in Figure 5; also see discussion in Paper I).

At time when $M_Z \approx 7.3 M_\oplus$ and $M_{XY} \approx 0.15 M_\oplus$, the

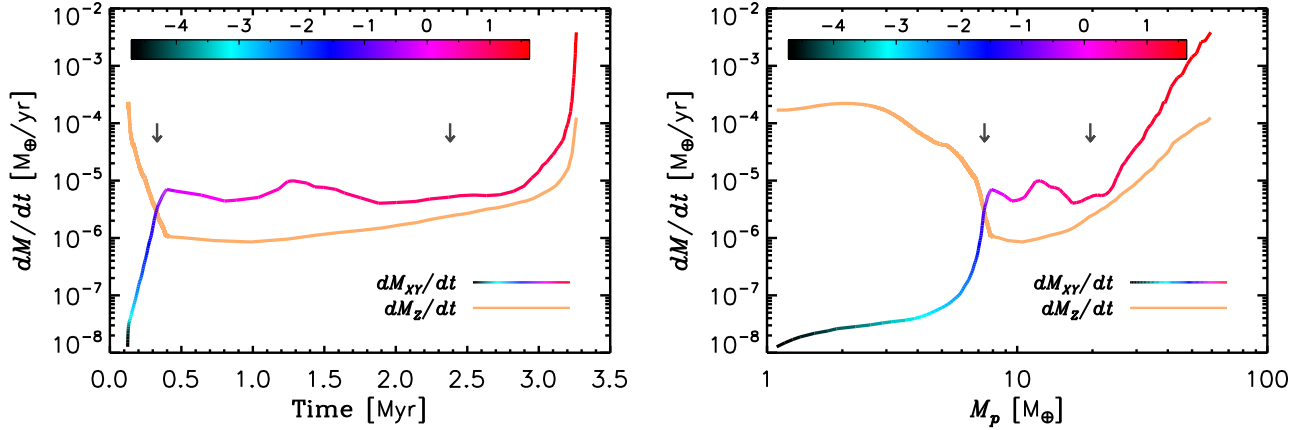


Figure 6: Accretion rate of heavy elements, dM_Z/dt , and of gas, dM_{XY}/dt , as a function of the time (left) and of the total planet mass (right). In both panels, the curve representing the gas accretion rate is color-coded by the logarithm of the envelope mass, M_{XY} , as indicated. Note that the evolution of the planet begins at $M_Z \approx 10^{-4} M_{\oplus}$ but the structure calculation of the envelope begins at $M_Z \approx 1 M_{\oplus}$. Phase 1 ends at $M_p \approx 7.45 M_{\oplus}$, when $\dot{M}_Z \approx \dot{M}_{XY} \approx 3 \times 10^{-6} M_{\oplus} \text{ yr}^{-1}$ (left arrow of pair). Phase 2 ends at $t \approx 2.38$ Myr, when $M_p \approx 19.6 M_{\oplus}$ (right arrow of pair).

accretion rates of H/He and heavier elements are approximately equal, $dM_Z/dt \approx dM_{XY}/dt \approx 3 \times 10^{-6} M_{\oplus} \text{ yr}^{-1}$. This formally signals the end of Phase 1 and the beginning of Phase 2. The behavior of both quantities can be seen in Figure 6, as a function of time (left) and planet mass (right, see figure's caption for details). The arrows mark the end of Phases 1 (left of pair) and 2 (right of pair). The figure also shows $\log(M_{XY}/M_{\oplus})$ color-coded on the gas accretion rate curves. The mass fraction of H/He at the end of Phase 1 is 2%. The growth from the initial embryo ($M_p \approx 10^{-4} M_{\oplus}$) to $M_p \approx 7.45 M_{\oplus}$ takes approximately 3×10^5 years, although the length of Phase 1 should also include the time needed to assemble the initial embryo.

The trend of dM_{XY}/dt and dM_Z/dt at the end of Phase 1 continues into Phase 2 for $\approx 10^5$ years, until $dM_{XY}/dt \approx 7 \times 10^{-6} M_{\oplus} \text{ yr}^{-1}$ and $dM_Z/dt \approx 10^{-6} M_{\oplus} \text{ yr}^{-1}$, when the total mass of the planet is $M_p \approx 8 M_{\oplus}$ ($M_{XY} \approx 0.6 M_{\oplus}$). During the next $\approx 2 \times 10^6$ years, the accretion rate of gas is relatively constant, as can be seen in Figure 6 and deduced from the near-linear growth of M_{XY} in Figure 5. The accretion of solids stays constant over the first $\approx 5 \times 10^5$ years of Phase 2 but it then begins to increase as the planet mass grows. During Phase 2, the planet adds nearly $10 M_{\oplus}$ of H/He and about $2.7 M_{\oplus}$ of heavy elements. Large bodies continue to deliver most of the heavy elements to the planet: by the time $M_Z \approx 10 M_{\oplus}$, about 66% of the high- Z material has been delivered by planetesimals $\gtrsim 10$ km in radius (but only $\approx 1\%$ by bodies with $R > 160$ km) and about 21% by bodies smaller than 1 km in radius.

As mentioned above, the accretion rates of H/He and heavy elements are correlated during Phases 1 and 2 (and the first part of Phase 3, see Figure 6), when envelope contraction is thermally regulated. While the planet is transitioning between Phases 1 and 2, $6 M_{\oplus} \lesssim M_p \lesssim 8 M_{\oplus}$, there is a large increase in dM_{XY}/dt (by almost two orders of mag-

nitudes) triggered by a large drop in dM_Z/dt . Likewise, during the latter part of Phase 2, dM_{XY}/dt declines by a factor of a few as dM_Z/dt increases by a similar factor. Fluctuations in the relative amounts of small planetesimals ($R \lesssim 0.1$ km) delivered to the envelope may also contribute to opacity, and hence dM_{XY}/dt , variations in Phase 2 (the outer envelope's layers are radiative during this Phase).

Cross-over mass ($M_{XY} = M_Z$) is attained at $t \approx 2.4$ Myr, when M_Z is around $10 M_{\oplus}$ (but see details in the caption of Figure 5). At that time, $dM_{XY}/dt \approx 5.5 \times 10^{-6} M_{\oplus} \text{ yr}^{-1}$, which is about twice as large as the accretion rate of heavy elements, $dM_Z/dt \approx 2.6 \times 10^{-6} M_{\oplus} \text{ yr}^{-1}$.

3.2. Phase 3

Past the end of Phase 2, the accretion rate of gas remains roughly constant until $M_p \approx 23 M_{\oplus}$ ($t \approx 2.7$ Myr), at which point it begins to increase in a runaway fashion, as illustrated in Figure 6.

Figure 7 shows the luminosity of the planet as a function of time (left) and total planet mass (right). The curves are also color-coded according to $\log(M_{XY}/M_{\oplus})$ in both panels. During Phase 1 the luminosity of the planet is close to the energy per unit time released by the accretion of heavy elements

$$L_Z \approx \frac{GM_Z(dM_Z/dt)}{R_Z}. \quad (6)$$

But also during Phase 2 and somewhat beyond, in the first part of Phase 3, the planet's luminosity can be approximated by L_Z . Equation (6) assumes that incoming planetesimals deliver most of their mass close to the core-envelope boundary, R_Z . This is not necessarily the case, since bodies can be consumed and/or break up farther above in the envelope. However, since most mass is delivered by large planetesimals (several tens of kilometers in radius), even toward and past

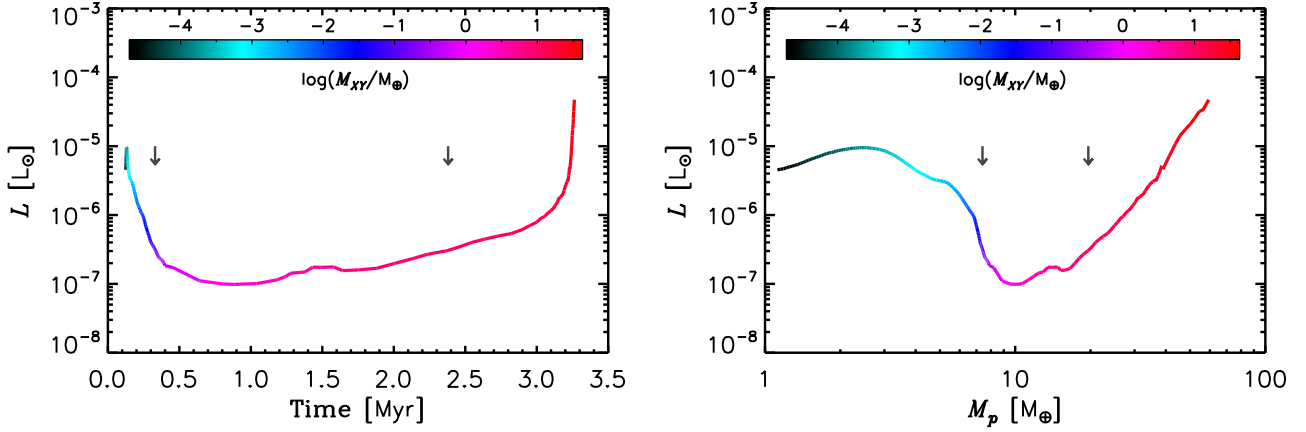


Figure 7: Luminosity of the planet as a function of the time (left) and of the total mass of the planet (right). The curves are color-coded by the logarithm of the envelope mass, M_{XY} . During Phase 1, the luminosity peak occurs when $M_p \approx 2.5 M_\oplus$ (see right panel). The transitions between Phases 1 and 2 and between Phases 2 and 3 are marked by the pair of arrows (see also Figure 6).

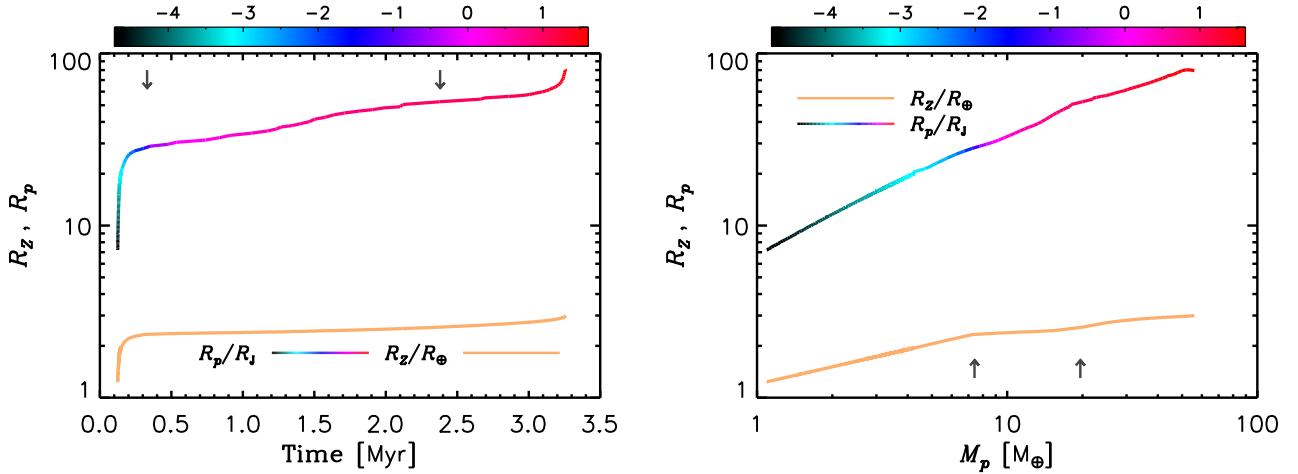


Figure 8: Radius of the planet, R_p , and radius of the heavy-element core, R_Z , respectively normalized to Jupiter's radius, R_J , and to the Earth's radius, R_\oplus ($R_J \approx 11 R_\oplus$). The radii are plotted as a function of the time (left) and of the total mass of the planet (right). The curve representing the planet's radius is color-coded by $\log(M_{XY}/M_\oplus)$. The transitions between Phases 1 and 2 and between Phases 2 and 3 are marked by the pair of arrows (see also Figure 6). Note that, throughout the epoch shown, the ratio R_p/R_Z increases from roughly 65 to 300.

the end of Phase 2 (see Figure 4) and large bodies tend to be held together by their own gravity, it is expected that accreted planetesimals release gravitational energy deep in the envelope. In the calculation, L is close to L_Z during these stages also because all accreted solids are assumed to eventually sediment onto the core.

The radius of the planet, i.e., the envelope radius, R_p is plotted in Figure 8, along with the radius of the heavy-element core R_Z , as a function of both time (left) and planet mass (right). The radii are normalized, respectively, by Jupiter's mean radius (at 1 bar envelope depth), $R_J = 69\,911$ km (Archinal et al., 2011), and by the Earth's radius, R_\oplus . The planet radius is also color-coded in terms of the envelope mass. As mentioned above, since the core is assumed to be incompress-

ible, $R_Z \propto M_Z^{1/3}$ (see Section 2). During Phases 1, 2, and 3 the envelope is in contact with the nebula and R_p is basically given by the effective radius R_{eff} , defined in Section 2.1. In the model, and throughout most of the evolution shown in the figure, R_{eff} is limited by $R_H/4$ (except for the early stages of Phase 1). The envelope starts to shrink when the rate of gas supply dictated by contraction exceeds that actually delivered by the nebula, which occurs somewhat later, during Phase 4 (see also Lissauer et al., 2009).

In Figure 9 we compare accretion rates (left) and luminosity (right) of the calculation discussed here (solid curves) with the results from the model labelled $\sigma 10$ of Movshovitz et al. (2010). That model also applied a density of solids $\sigma_Z^0 = 10 \text{ g cm}^{-2}$ at $a = 5.2$ au. However, that calculation did

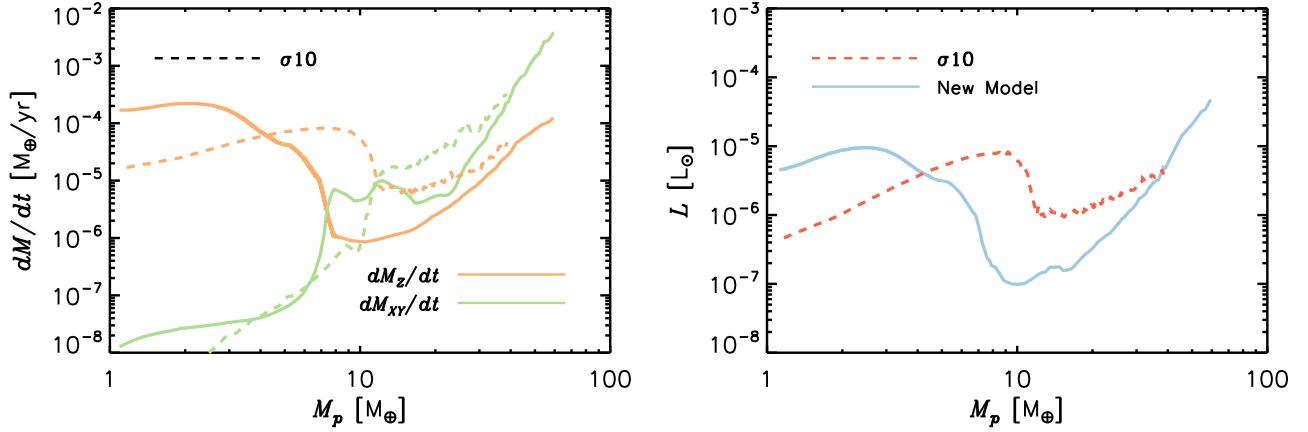


Figure 9: Comparison of the accretion rates of heavy elements and gas (left) and luminosity (right), as a function of the total planet mass, for the new calculation (solid lines) and a model from Movshovitz et al. (2010), labelled as $\sigma10$ (dashed lines), as indicated in the legends (see text for further details).

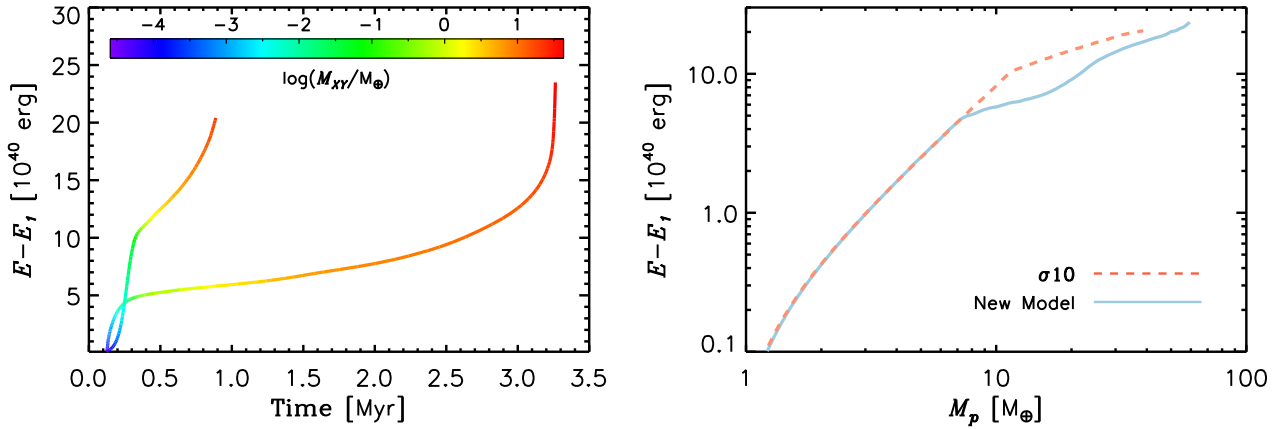


Figure 10: Cumulative energy radiated by the planet, Equation (7), as a function of time (left) and total mass (right). The plots in both panels compare the new formation model to model $\sigma10$ of Movshovitz et al. (2010) (see also Figure 9 and text for details), which completes Phase 2 in a little less than 1 Myr. For comparison purposes, the evolutionary track of model $\sigma10$ is shifted in time (see text). The curves of the left panel are color-coded by the value of M_{XY} .

not account for the evolution of the swarm of planetesimals, but it rather assumed an accretion rate of solids based on the three-body problem results of Greenzweig and Lissauer (1992), and planetesimals were assumed to be all 100 km in radius. Model $\sigma10$ achieves the $dM_Z/dt = dM_{XY}/dt$ condition, the end of Phase 1, at $M_p \approx 12.1 M_{\oplus}$, a mass larger than that in the new model, but when M_Z ($11.5 M_{\oplus}$) is close to the mass predicted by Equation (3) for a solid's feeding zone parameter $b = 4$. During Phase 2, the accretion rates of both gas and heavy elements in the previous model are on average several times as large, and so is the luminosity (as also predicted by Equation (6)). Phase 3 begins at $M_p \approx 32 M_{\oplus}$ in model $\sigma10$, a mass significantly larger than that in the current model. However, once into Phase 3, accretion rates and luminosity become comparable to those of the new model.

The cumulative energy radiated by the planet during formation

$$E(t) = \int_t L(M_p) dt', \quad (7)$$

where M_p is a function of time, is illustrated in Figure 10 for both the new model and model $\sigma10$ of Movshovitz et al. (2010). In the figure, the energy E_1 represents the cumulative energy radiated by the planet until its total mass is approximately $1 M_{\oplus}$. In this calculation, the planet growth starts when $M_p = M_Z \approx 10^{-4} M_{\oplus}$, although the envelope structure is calculated only for $M_Z > 1.1 M_{\oplus}$. Nonetheless, assuming that for $M_Z \lesssim 1 M_{\oplus}$ the luminosity L can be approximated by the accretion luminosity L_Z in Equation (6), an approximation that holds valid at far larger masses, it is estimated that $E_1 \approx 9 \times 10^{38}$ erg. The evolution of model $\sigma10$ is shifted in

time so that it achieves $M_Z \approx 1.1 M_\oplus$ at the same time as the new model. Since E_1 cannot be computed for model $\sigma 10$ (because that model was started at about $1.2 M_\oplus$), we assume the same value for E_1 . Notice that the evolution of model $\sigma 10$ is faster, completing Phase 2 in about 0.97 Myr (compare curves in left panel of Figure 10), when $M_p \approx 32 M_\oplus$. Nonetheless, the two models predict similar radiated energies up until $M_p \approx 7.5 M_\oplus$ (assuming comparable values for E_1), which marks the end of Phase 1 in the new model. The release of energy is larger on average in model $\sigma 10$ during Phase 2 and the initial stages of Phase 3, but they again appear to become comparable later on.

The structure calculation is continued up to a time $t \approx 3.3$ Myr, when $M_Z \approx 16.2 M_\oplus$. At that point, the total mass of the planet exceeds $60 M_\oplus$. During this time both dM_{XY}/dt and dM_Z/dt increase, but the rate of growth of the former greatly exceeds that of the latter (see Figure 6). Accretion of solids is still dominated by large bodies, as can be seen in Figure 4. By the time $M_Z \approx 16 M_\oplus$, about 74% of the heavy elements has been delivered by planetesimals larger than ≈ 10 km in radius and about 19% by bodies $\lesssim 1$ km in radius.

Proper runaway accretion of gas, defined as the mass-doubling timescale M_p/\dot{M}_p being a decreasing function of M_p , commences shortly after the start of Phase 3, when $M_p \approx 23 M_\oplus$. Even so, the planet takes over half a million years to double its mass (see Figure 5 and 6), a reminder that the onset of runaway gas accretion does not necessarily imply an immediately short growth timescale.

3.3. Phase 4

Once $M_p \gtrsim 65 M_\oplus$, envelope contraction allows gas accretion rates in excess of $0.01 M_\oplus \text{ yr}^{-1}$. These large values of dM_{XY}/dt may exceed the rate at which a disk (a few million years old at this point) can supply gas to the planet, unless the disk is initially very massive and/or very long-lived (in excess of several Myr). The planet would then have entered Phase 4, the phase of disk-limited gas accretion (D'Angelo and Lubow, 2008; Lissauer et al., 2009), whereby disk evolution and disk-planet tidal interactions limit the supply of gas that can be delivered to the vicinity of the planet.

In fact, the disk models presented below predict, at that time of the evolution ($t \approx 3.3$ Myr) and for models forming Jupiter-mass planets, disk-limited accretion rates of a few to several times $10^{-3} M_\oplus \text{ yr}^{-1}$, depending on the level of gas turbulence viscosity (see Figure 11). These accretion rates are comparable with the values dictated by envelope contraction in the structure calculation when $M_p \approx 60 M_\oplus$, as indicated in Figure 6. At that point of the evolution, $M_Z \approx 16 M_\oplus$ and the heavy-element accretion rate is $\approx 10^{-4} M_\oplus \text{ yr}^{-1}$.

In order to simulate the evolution in Phase 4 until the planet achieves its final mass, we consider the results from the structure calculation discussed above up to a time between 3.2 and 3.3 Myr (see Figure 5), when $M_Z \approx 16 M_\oplus$ and the total mass of the planet is $M_p \approx 60 M_\oplus$.

For increasing planet masses not satisfying the inequal-

ity in Equation (5), disk-limited accretion is first of ‘‘Bondi-type’’, $\dot{M}_{XY} \propto M_p^3$, and then of ‘‘Hill-type’’, $\dot{M}_{XY} \propto M_p$ (D'Angelo and Lubow, 2008). Typically, however, these regimes can provide accretion rates larger, or much larger, than cooling-limited accretion does at those planet masses. Once the condition (5) is satisfied, \dot{M}_{XY} is a relatively weak function of planet mass at first, and then it rapidly declines as M_p increases.

The mass growth of the planet in Phase 4 is calculated by integrating the disk-limited accretion rates computed by Lissauer et al. (2009) and Bodenheimer et al. (2013). The integration starts at the point when gas accretion dictated by contraction exceeds disk-limited accretion, according to the local disk conditions. The calculation proceeds as follows. It is assumed that, during its evolution, the planet orbits at a fixed distance ($a = 5.2$ au) from the Sun. The nebula gas has a viscosity parameter, α (Shakura and Sunyaev, 1973), constant both in space and time. Given an initial ($t = 0$) gas surface density, $\Sigma \propto a_p/a$ (with an exponential cut-off beyond ≈ 40 au), where a is again the heliocentric distance, gas is removed from the disk by accretion on the planet dM_{XY}/dt , accretion on the Sun $\dot{\mathcal{M}}_v$, and photo-evaporation (i.e., disk wind) $\dot{\mathcal{M}}_w$.

The accretion through the disk and onto the Sun, driven by viscous diffusion, is modeled by assuming steady-state conditions (Pringle, 1981),

$$\frac{d\mathcal{M}_v}{dt} = 3\pi\nu\Sigma, \quad (8)$$

in which $\partial(\nu\Sigma)/\partial a \approx 0$. Here ν represents the kinematic viscosity and is given by $\nu = \alpha H^2\Omega$, where H is the pressure scale-height of the nebula and $\Omega = \sqrt{GM_\odot/a^3}$ the local Keplerian frequency. The disk's thermal structure is such that $H \propto a^{9/7}$ (e.g., Chiang and Youdin, 2010), which makes ν nearly proportional to the heliocentric distance. The photo-evaporation rate is assumed to be constant, both in time and space, with $\dot{\mathcal{M}}_w \approx 10^{-8} M_\odot \text{ yr}^{-1}$ (e.g., Gorti et al., 2016; Picogna et al., 2019). The gas density at the orbital distance of the planet is calculated from the total disk mass \mathcal{M}_D , as the disk depletes, by preserving the initial slope $d \ln \Sigma / d \ln a$ of the distribution:

$$-\frac{d\mathcal{M}_D}{dt} = \frac{d\mathcal{M}_v}{dt} + \dot{\mathcal{M}}_w + \frac{dM_{XY}}{dt} \quad (9)$$

and $\Sigma(a_p, t) \propto \mathcal{M}_D(t)/(\pi a_p^2)$. Preservation of $d \ln \Sigma / d \ln a$ with time stems from the fact that, in a steady-state disk, Σ is nearly proportional to $1/\nu$. The mass M_p is integrated until $\mathcal{M}_D = 0$. In Phase 4 it is also assumed that $\dot{M}_p = \dot{M}_{XY}$, a reasonable approximation since the gas accretion rate can be a factor of 10, or more, larger than the accretion rate of heavy elements around the onset of disk-limited accretion, and the ratio increases as M_p grows (assuming that accretion of solids is only caused by expansion of the feeding zone, see Equation (4)).

The disk models also assume that the initial reservoir of solids from which the planet forms is the same as in Equation (2), independently of the initial value adopted for the

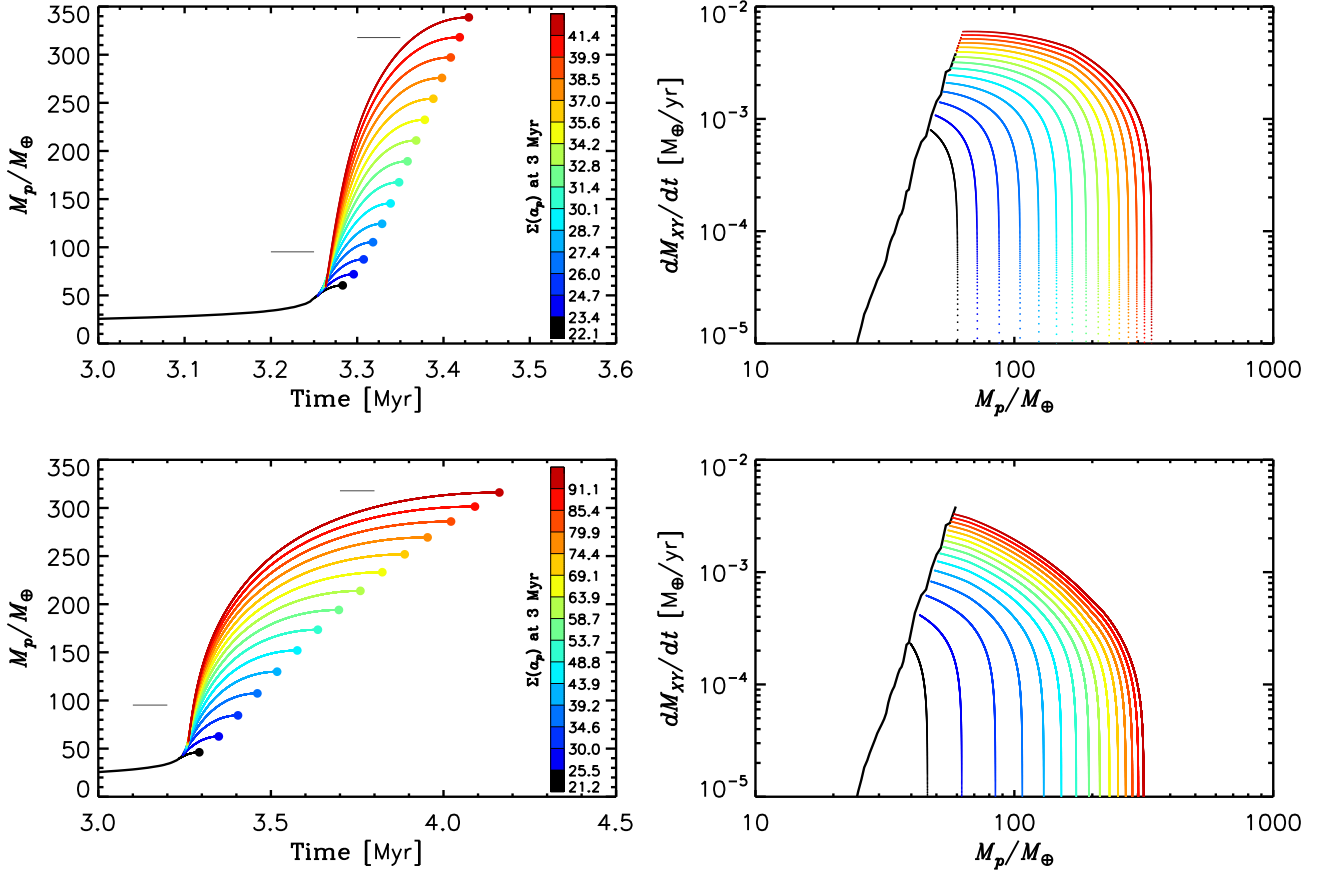


Figure 11: Left: Growth tracks of the planet undergoing disk-limited accretion during Phase 4. The solid circles indicate the final mass when the nebula around the planet's orbit has dispersed. Different colors indicate different values of the disk mass, \mathcal{M}_D , at $t = 0$. The curves are color-coded according to the value of the gas density at the planet location, $\Sigma(a_p)$ in g cm^{-2} , after 3 Myr. The lower and upper horizontal segments to the left of the tracks indicate, respectively, the masses of Saturn and Jupiter. Right: Gas accretion rate versus planet mass for the same models as in the left panels. The turbulence viscosity parameter of the nebula is $\alpha = 4 \times 10^{-3}$ in the top panels and $\alpha = 4 \times 10^{-4}$ in the bottom panels. Thick black curves represent results from the structure calculations, in which accretion is limited by the envelope's thermal pressure.

local gas surface density. This is not a global attribute of the disk (the solid component is not modeled), but rather a local property, spanning a few au in radius over the planet formation region. Globally (i.e., over tens of au) the initial total mass of solids may still be related to the initial total mass of gas.

Neglecting gas removal by planetary accretion, the computed lifetime of such a nebula model would be ≈ 3.5 Myr for $\alpha = 4 \times 10^{-3}$ and an initial disk mass of $0.1 M_\odot$. For $\alpha = 4 \times 10^{-4}$, the lifetime would be ≈ 8 Myr, as mostly determined by the factor of 10 difference in α (the disk dispersal timescale is $\propto \alpha^{-1/3}$ for a constant $\dot{\mathcal{M}}_w$, e.g., Gorti et al., 2015). At the latter viscosity level, an initial nebula whose mass was $0.05 M_\odot$ would last ≈ 4.4 Myr.

The evolution of the planet mass is found by solving the differential equation

$$\frac{dM_p}{dt} = \Psi(M_p, a_p, H, \alpha)\Sigma(a_p, t), \quad (10)$$

where Ψ is a parametric function of α derived from three-

dimensional hydrodynamic simulations (Lissauer et al., 2009; Bodenheimer et al., 2013). The local value of the gas surface density $\Sigma(a_p, t)$ depends on $\mathcal{M}_D(t)$, which is determined by integrating Equation (9). Equation (10) is solved numerically by means of an Adams-Bashforth-Moulton method of variable order with adaptive step-size and error control. The initial time at which the integration starts is taken from the structure calculation as the time at which the right-hand side of Equation (10) drops below the rate of accretion dictated by contraction (see Figure 6). If a disk model predicts gas accretion rates on the planet greater than that in Figure 6 when $M_p = 60 M_\oplus$, we apply an extrapolation of dM_{XY}/dt obtained from the structure calculation data. More specifically, we use a linear regression in $\log \dot{M}_{XY} - \log M_p$ space, in the range $M_p = 25 - 60 M_\oplus$. The extrapolated dM_{XY}/dt is applied until it exceeds the disk-limited accretion rate, i.e., the right-hand side of Equation (10). Note that, as long as the planet is in contact with the nebula, i.e., during Phases 1 through 3, the gas disk model (of the type considered here) is not expected to affect its evolution much.

Results from the mass integration under the assumption of disk-limited accretion are plotted in Figure 11. The left-top panel shows the growth tracks of the planet in disks whose initial mass varies between 0.089 and 0.102 M_{\odot} and $\alpha = 4 \times 10^{-3}$. The left-bottom panel shows models in which the planet grows in less viscous disks, $\alpha = 4 \times 10^{-4}$, whose initial mass varies between 0.036 and 0.048 M_{\odot} . The gas surface density after 3 Myr, at the radial location of the planet, $\Sigma(a_p)$, is indicated in the left panels in units of g cm^{-2} . Solid circles mark track ends, when $\Sigma(a_p) = 0$. The right panels of the figure show the gas accretion rate as a function of the planet mass for the same cases as in the left panels. In the Figure, the transition between Phases 3 and 4 occurs at the beginning (leftmost positions) of the colored curves, and is dependent on the disk model.

In the models illustrated in the top panels, corresponding to more viscous disks, the initial density ($t = 0$) at the planet orbit ranges from ≈ 630 to $\approx 730 \text{ g cm}^{-2}$, yielding an initial gas-to-solids mass ratio comparable to that reported by Pollack et al. (1994). At $t = 3 \text{ Myr}$, $\Sigma(a_p)$ declines to values between ≈ 22 and $\approx 41 \text{ g cm}^{-2}$. The final mass of the planet after gas disperses ranges from 60 to 339 M_{\oplus} and is achieved between $t \approx 3.28$ and $\approx 3.43 \text{ Myr}$. Final masses similar to Jupiter's are achieved at $t \approx 3.42 \text{ Myr}$, one million years after the beginning of Phase 3 and $\approx 150\,000$ years after the beginning of Phase 4. The top-right panel of Figure 11 indicates that disk-limited accretion sets in at masses $M_p \lesssim 60 M_{\oplus}$ when the initial gas surface density around the planet's orbit is $\Sigma \lesssim 700 \text{ g cm}^{-2}$.

In the models corresponding to less viscous disks, illustrated in the bottom panels of Figure 11, $\Sigma(a_p)$ at $t = 0$ varies between ≈ 260 and $\approx 340 \text{ g cm}^{-2}$ whereas, after 3 Myr, the gas surface density at the planet's orbit drops to values between ≈ 21 and $\approx 91 \text{ g cm}^{-2}$. In these examples, the solids necessary to form the planet would initially be spread over a radial region about 2.5 times as wide as in the $\alpha = 4 \times 10^{-3}$ disks if the local gas-to-solids mass ratio was the same, hence requiring some redistribution during (or prior to) planet assembly. In the cases shown in the plot, the mass of the planet after gas dispersal ranges from 46 to 316 M_{\oplus} . Isolation starts between $t \approx 3.3$ and $\approx 4.2 \text{ Myr}$. At the latter time the planet would achieve a final mass similar to Jupiter's, 1.8 Myr after the beginning of Phase 3 and $\approx 930\,000$ years after the beginning of Phase 4. Owing to the decreased ability of the disk to deliver gas to the planet, which arises from the combination of a smaller accretion rate, dM_p/dt , and deeper tidal gap at any given planet mass, disk-limited accretion sets in prior to $M_p \approx 60 M_{\oplus}$ for the models considered here (see bottom-right panel).

We apply the same modeling procedure to choose an initial ($t = 0$) gas surface density that would result in a final mass equal to Jupiter's, for three different values of the turbulence parameter $\alpha = 4 \times 10^{-4}$, 10^{-3} , and 4×10^{-3} . Results are shown in Figure 12. In these models, the initial $\Sigma(a_p)$ ranges from 339 to 722 g cm^{-2} , for increasing values of α , and formation is complete between $t \approx 3.42$ and 4.17 Myr. The initial disk (gaseous) mass is somewhat less than 0.05 M_{\odot} in the

two less viscous cases and 0.1 M_{\odot} in the highest viscosity case. In all cases, the formation time is consistent with observational estimates of *dust* lifetimes in circumstellar disks (e.g., Gorti et al., 2016; Ercolano and Pascucci, 2017, and references therein).

At the level of viscosity considered in the models displayed in Figure 11 and 12, the accretion rate of gas declines with time when disk-limited accretion sets in because, at those planet masses, disk-limited accretion is already past its maximum, $\partial\Psi/\partial M_p < 0$ in Equation (10) (see e.g., Lissauer et al., 2009; Bodenheimer et al., 2013), and also because Σ declines with time. For a given surface density, disk-limited rates start to decline for M_p satisfying Equation (5) (within a factor of order unity), which occurs at several tens of Earth's masses ($\alpha = 4 \times 10^{-3}$) or less ($\alpha = 4 \times 10^{-4}$).

The right panel of Figure 12 indicates that disk-limited accretion starts when $M_p \approx 58 M_{\oplus}$ for the two cases with lowest viscosity, and that it starts earlier when $\alpha = 0.001$. This implies that disk-limited accretion is (somewhat) lower at that planet mass when $\alpha = 0.001$. But since Ψ in Equation (10) is smaller for $\alpha = 4 \times 10^{-4}$ than it is for $\alpha = 0.001$, the difference is caused by the lower surface density $\Sigma(a_p)$ at intermediate viscosity at the epoch when disk-limited accretion begins.

By applying the same turbulence viscosity as in the models displayed in Figure 12, we integrate the disk-limited accretion rates of the right panel for a number of initial disk masses, $\mathcal{M}_D(0)$. As mentioned above, the gaseous nebula is supposed to extend over a radial distance of roughly 50 au. Results are plotted in Figure 13 for the final mass of the planet, M_p^f , as a function of t_{disk} , the nebula lifetime. Different symbols indicate the three different levels of turbulence viscosity (see legend) and colors render $\mathcal{M}_D(0)$. Within a timescale $\lesssim 5 \text{ Myr}$, giant planets more massive than several times Jupiter's mass (M_J) can more easily form when gas viscosity is high. Low viscosity ($\alpha \ll 0.001$) disks are generally incapable of forming gas giants exceeding $\approx 2 M_J$, despite the fact that they can live much longer (for equal values of $\mathcal{M}_D(0)$). As a reference, for the largest value of the disk mass used and $\alpha = 4 \times 10^{-4}$, the planet's final mass is $M_p^f \approx 2.25 M_J$ and it would still be $< 2.5 M_J$ even if $\mathcal{M}_D(0)$ was 0.2 M_{\odot} . It should be noted that, even though observations seem to suggest that average timescales for dust removal from disks are in the range 3–5 Myr, gas dispersal timescales could be longer (e.g., Gorti et al., 2016; Ercolano and Pascucci, 2017).

3.3.1. Planetary Structure During Phase 4

The structure and evolution of the planet during the phase of disk-limited accretion is calculated by applying the gas accretion rates plotted in the right panel of Figure 12, for the two cases with $\alpha = 4 \times 10^{-3}$ and 4×10^{-4} , referred to as models $\alpha 43$ and $\alpha 44$, respectively. The structure calculation still assumes hydrostatic equilibrium, and the accreting gas is assumed to impact the planet's surface at a velocity close to free-fall, v_{ff} . The density at R_p is derived from the gas accretion rate and the free-fall velocity, $\propto \dot{M}_{XY}/(R_p^2 v_{\text{ff}})$.

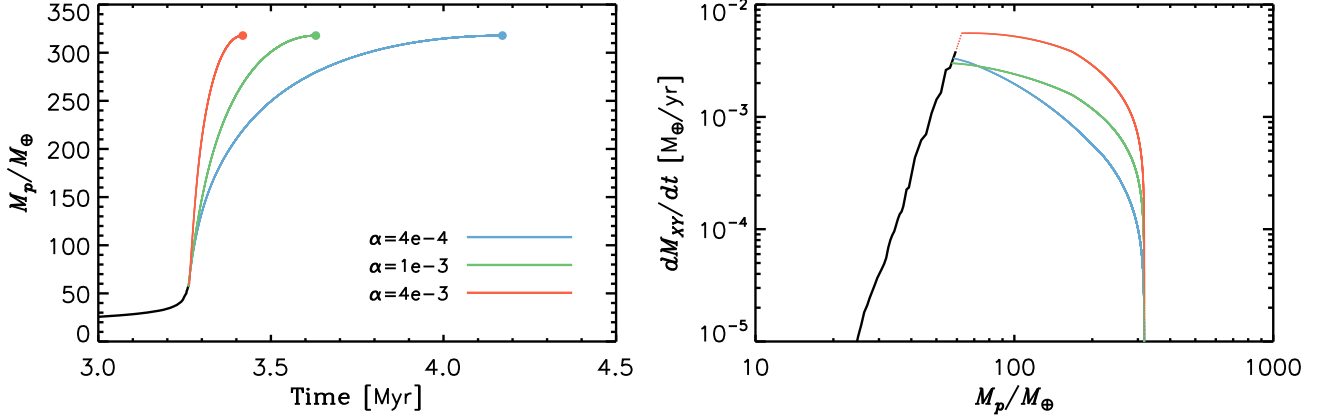


Figure 12: Growth tracks and accretion rates as in Figure 11, for three different values of the turbulence viscosity parameter α , as indicated. The initial disk mass is chosen as to result in a final planet mass (after disk dispersal) equal to Jupiter's (see text for further details).

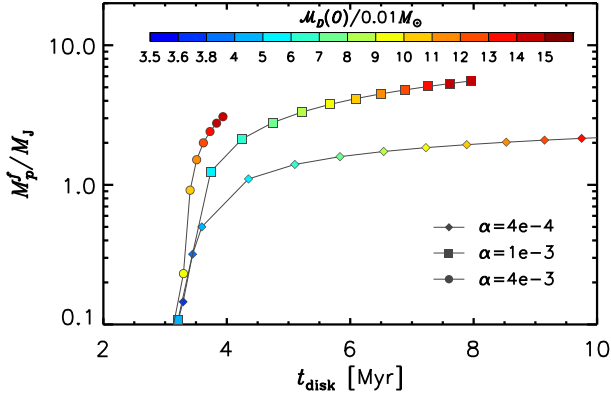


Figure 13: Final mass of a planet, M_p^f , versus the disk's gas lifetime, t_{disk} . The vertical axis is in units of Jupiter's mass, M_J . Different symbols indicate different values of the turbulence parameter α in the disk, as reported in the legend. Each symbol is color-coded according to the initial value of the disk mass $M_p(0)$, as indicated in the color bar in units of $0.01 M_\oplus$.

The temperature at the surface is determined by an approximate solution of the radiation diffusion equation, applying the total luminosity of the planet (produced by contraction and accretion). Quantitative details can be found in Bodenheimer et al. (2000).

In this phase, the accretion of solids assumes continued supply of planetesimals from the edges of the gap in the solids' distribution (see Figure 1), according to Equation (4). The accretion rate of heavy elements can therefore be written in terms of the gas accretion rate, as

$$\frac{dM_Z}{dt} = \left(\frac{C}{M_p^{2/3} - C} \right) \frac{dM_{XY}}{dt}. \quad (11)$$

The constant is chosen by using the ratio \dot{M}_Z/\dot{M}_{XY} prior to the onset of disk-limited accretion, at the largest core mass for which the swarm of solids is evolved ($M_Z \approx 16 M_\oplus$).

The size distribution of accreted planetesimals does not change during this phase and accretion rates as a function of planetesimal radius are obtained by re-scaling the solids' mass in each size bin by \dot{M}_Z in Equation (11). The relative contributions versus R are thus constant during the evolution, and most of the heavy elements continue to be delivered by planetesimals larger than 10 km in radius (see Figure 4). Because of ongoing accretion of solids, envelope-planetesimal interaction calculations, including the calculation of grain opacity, are also performed during this phase (see Section 2.1).

The total mass of heavy elements at the end of Phase 4 (when $M_p = 1 M_J$) is $M_Z \approx 20 M_\oplus$, similar in the two cases because the ratio \dot{M}_Z/\dot{M}_{XY} at the end of Phase 3 (i.e., constant C in Equation (11)) is comparable (note that the beginning of Phase 4 is somewhat different in the two models, see Figure 12). The planet would collect this amount of solids if, according to Equation (3), it cleared planetesimals from a region of radial width $\approx 2.3 R_H$ on either side of its orbit. Direct calculations performed by D'Angelo and Podolak (2015) indicate that, for a Jupiter-mass planet, $b \approx 2.5$ on average for $R \gtrsim 1$ km planetesimals (which provide the bulk of the heavy-element mass in these models).

A variant of model $\alpha 43$ is also considered, in which the supply of solids is assumed to end around the epoch when disk-limited accretion begins (model $\alpha 43LZ$). In this model the total mass of heavy elements at the end of formation is $M_Z = 16.1 M_\oplus$. Once accretion of solids stops, there is no energy delivery by incoming planetesimals. Thereafter, it is assumed that dust grains in the outer envelope are only supplied by the gas accretion flow and the opacity calculation follows the approach of D'Angelo and Bodenheimer (2016).

Maximum rates of gas accretion are $\dot{M}_{XY} \approx 3.3 \times 10^{-3}$ and $\approx 5.6 \times 10^{-3} M_\oplus \text{ yr}^{-1}$, respectively in the less and more viscous nebula. Correspondingly, maximum accretion rates of heavy elements are $\dot{M}_Z \approx 1.2 \times 10^{-4}$ and $\approx 1.7 \times 10^{-4} M_\oplus \text{ yr}^{-1}$. During this phase, as the planet mass grows by a factor of ≈ 5.5 , the heavy-element mass increases by 25% at most. Apart from compositional changes

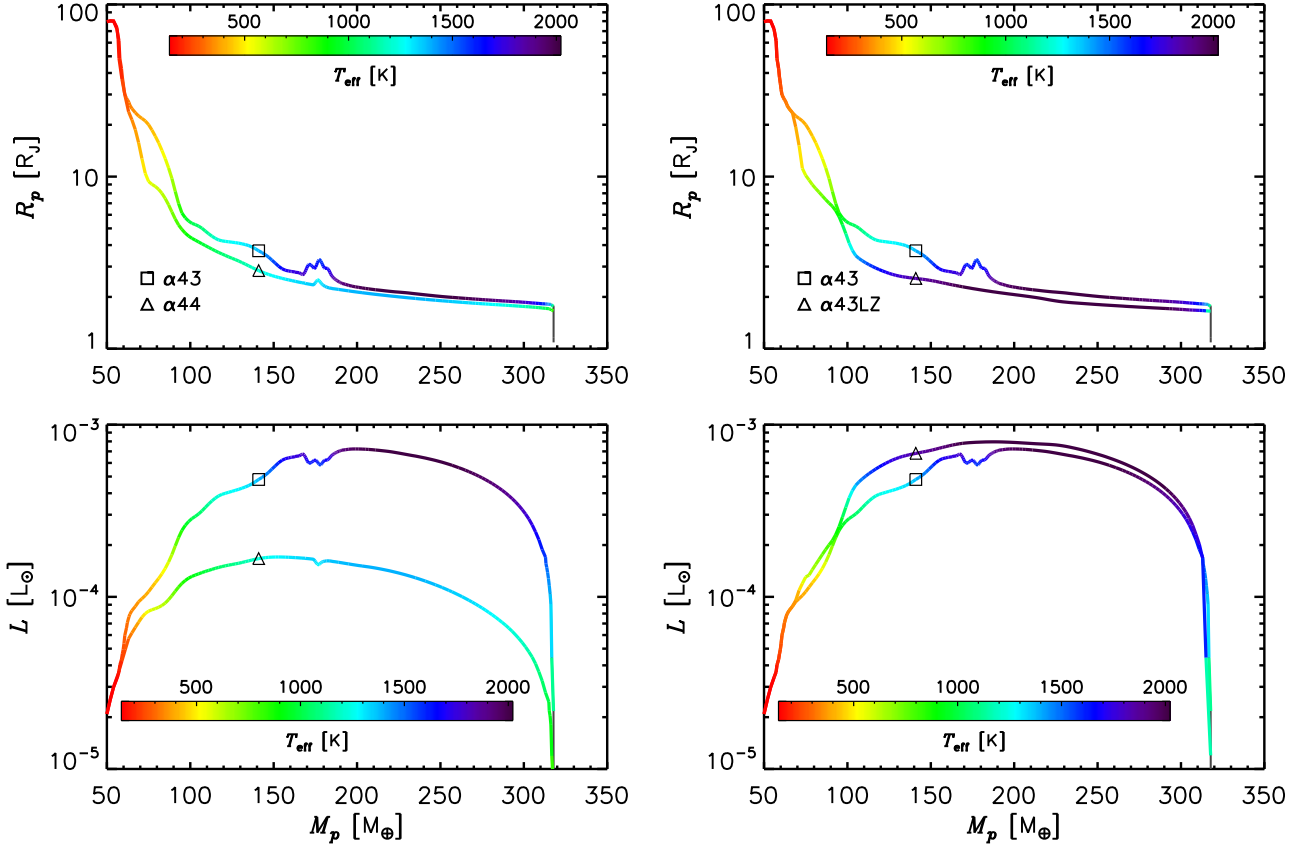


Figure 14: Evolution of the planet during disk-limited accretion, according to disk models described in Section 3.3 and presented in Figure 12. Model $\alpha 43$ and $\alpha 44$ refer, respectively, to the nebula models with turbulence parameter $\alpha = 4 \times 10^{-3}$ and 4×10^{-4} (see legends in the top panels). Model $\alpha 43LZ$ refers to a variation of model $\alpha 43$, with lower heavy element content (see text). The planet radius (top) and luminosity (bottom) are plotted as a function of the planet mass. The color bar renders the effective temperature of the planet T_{eff} , Equation (12). The transition between Phase 3 and 4 slightly depends on the applied disk model (see Figure 12). The dark-gray (vertical) portion of the curves represents the isolation phase (see Section 3.4).

in the interior, most of the impact of solids' accretion during this time is due to the dust contribution to the opacity of the outer envelope's layers, which can affect contraction.

Results for the evolution of the planet radius and luminosity during the disk-limited accretion phase are presented in Figure 14. Dark-gray (vertical) portions of the curves represent evolution during the isolation phase, described in Section 3.4. As soon as the accretion rate of gas cannot keep up with the contraction rate of the envelope, the planet starts to shrink. In doubling its mass, from $M_p = 50$ to $100 M_\oplus$, the radius reduces by a factor of ≈ 16 , a contraction in volume of over 4000 times (i.e., by more than 99.97%). And by the end of formation, the planet's volume shrinks another 96%. The radius R_p at the end of Phase 4 is comparable in the three models, ranging from $1.65 R_J$ (model $\alpha 43LZ$) to $1.76 R_J$ (model $\alpha 43$).

As expected, the luminosity is lowest in model $\alpha 44$ during most of the disk-limited accretion phase (see bottom panels), because of the relatively slow rate at which energy is supplied by gas accretion (this part of formation in model $\alpha 44$ lasts several times as long as in the other models, see left panel of

Figure 12). For $M_p > 100 M_\oplus$, the luminosity of model $\alpha 43$ is between 2 and 6 times as large as that of model $\alpha 44$, when compared at the same planet mass, and about 2.6 as large at the end of Phase 4.

Model $\alpha 43LZ$ is more luminous than model $\alpha 43$ (but by $\lesssim 50\%$) during most of the disk-limited accretion phase, likely due to its less opaque outer envelope (therefore the planet also contracts somewhat faster initially, see top-right panel). However, the cooling rate slows down as M_p grows (note that energy delivered by gas accretion versus planet mass is similar in the two models) and, by the end of Phase 4, L drops below the luminosity of model $\alpha 43$ (see Figure 14, bottom-right panel). According to these models, at the end of formation the young Jupiter is between several 10^3 and 10^4 times as luminous as it is today.

The curves in Figure 14 are color-coded in terms of the effective temperature of the planet, defined by

$$L = 4\pi\sigma_{\text{SB}}R_p^2T_{\text{eff}}^4, \quad (12)$$

where σ_{SB} is the Stefan-Boltzmann constant. The effective temperature peaks at ≈ 2000 and ≈ 2200 K, respectively, in

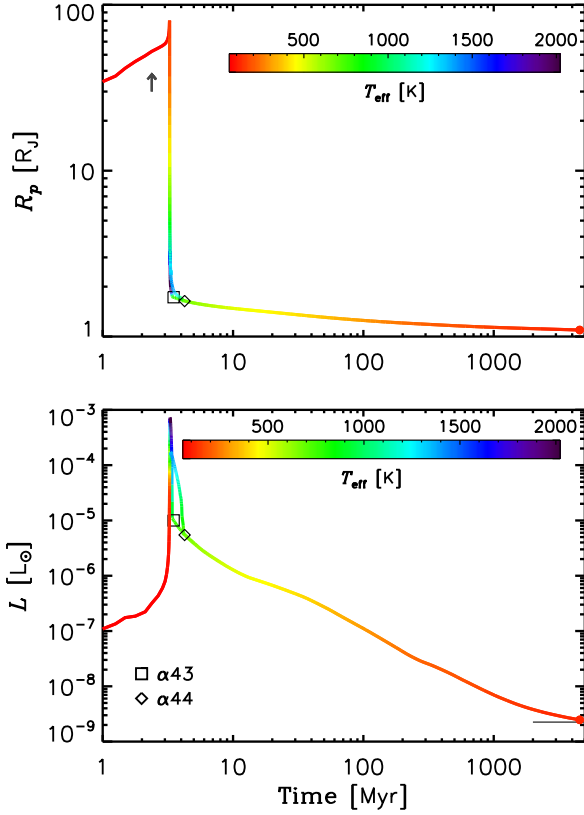


Figure 15: The same quantities as in Figure 14 are plotted for models $\alpha 43$ and $\alpha 44$ as a function of time, starting from Phase 2 and continuing to the present epoch. Phase 2 ends at $t \approx 2.38$ Myr in both cases (see arrow); Phase 3 ends at $t \approx 3.3$ Myr, with a slight dependence on the disk model (see Figure 12). The square and diamond symbols indicate the end of Phase 4 in the two models (see legend in the bottom panel). The solid circles mark the age of the solar system, $t = 4567$ Myr. The color bar renders the planet's effective temperature (see Equation (12)). During the isolation phase the two models are hardly distinguishable. The horizontal segment in the bottom panel indicates Jupiter's current luminosity (see text).

models $\alpha 43$ and $\alpha 43LZ$. In the less viscous nebula model, T_{eff} has a maximum at 1400 K. However, the planet in model $\alpha 44$ remains “warm” ($T_{\text{eff}} > 1000$ K) for about 7×10^5 years, a long period of time compared to only 1.4×10^5 years in models $\alpha 43$ and $\alpha 43LZ$. In all three cases, this state lasts from when $M_p \approx 100 M_{\oplus}$ until formation is nearly complete. At the end of Phase 4, T_{eff} ranges between ≈ 750 (model $\alpha 44$) and ≈ 940 K (model $\alpha 43$).

3.4. Isolation Phase

The evolution during the isolation phase is calculated until $t \approx 5000$ Myr, somewhat longer than the reference age of the solar system, 4567 Myr (Connelly et al., 2012). Standard photospheric boundary conditions (e.g., Weiss et al., 2006; Kippenhahn et al., 2013) are applied in this phase, as the planet cools and contracts, and the envelope is assumed to be free of dust.

During isolation, the energy absorbed from the Sun can provide a significant contribution to the thermal state of the upper envelope, and hence it may alter the contraction of Jupiter. Solar irradiation is taken into account following the approach outlined in D’Angelo and Bodenheimer (2016). The energy flux impinging on the planet and absorbed by the envelope is parameterized in terms of an “equilibrium” temperature T_{eq} , such that

$$4\sigma_{\text{SB}}T_{\text{eq}}^4 = \frac{L_{\odot}}{4\pi a^2}(1 - \mathcal{A}), \quad (13)$$

where \mathcal{A} represents the planet’s albedo. The total luminosity of the planet is then written as

$$L = L_{\text{int}} + 4\pi\sigma_{\text{SB}}R_p^2T_{\text{eq}}^4. \quad (14)$$

Loosely speaking, the internal luminosity L_{int} is the power generated by internal energy sources, which the planet would have if it was not irradiated by the Sun. Strictly speaking, the irradiation flux applied to the top part of the envelope can affect the temperature structure in the underlying layers and, therefore, L_{int} can also depend on T_{eq} , although the effect is expected to be small in the case of Jupiter. According to Equation (12) and Equation (14), T_{eff} would converge to T_{eq} as the planet cools.

We use a present-day value for Jupiter’s albedo $\mathcal{A} = 0.343$, based on Pioneer and Voyager 1 observations (Hanel et al., 2003), and for the Sun’s luminosity (L_{\odot}), which correspond to a constant $T_{\text{eq}} \approx 110$ K. This approximation somewhat overestimates the second term on the right-hand side of Equation (14) since the Sun’s luminosity has risen by about 30% over the past 4000 Myr (Ribas, 2010; Spada et al., 2013). The consequences are quantified in Appendix A, where results are presented of a version of model $\alpha 43$ that uses a time-dependent solar irradiation. Results from using an alternative value for the albedo are also discussed in the Appendix.

Figure 15 shows the evolution of Jupiter’s radius and luminosity during most of the planet’s history, including most of Phase 2 as well as Phases 3, 4, and the isolation phase (see caption of Figure 15 for further details). Only models $\alpha 43$ and $\alpha 44$ are plotted (see legend in the bottom panel). Their behavior is very similar during the isolation phase, and very similar to that of model $\alpha 43LZ$. The curves are again rendered according to T_{eff} . Square and diamond symbols mark the end of Phase 4 in the two models, whereas the solid circles on the right-hand ends of the curves mark the age of the solar system.

Although the three models begin the isolation phase with luminosities differing by a factor of ≈ 1.8 (R_p differs by much less, about 7%), L is basically the same by $t = 30$ Myr. Thereafter, the models can be hardly distinguished. At the age of the solar system, model variations in radius and luminosity are below 1%, with $R_p = 1.09 R_J$, $L = 2.47 \times 10^{-9} L_{\odot}$, about 10% in excess of Jupiter’s average emitted power ($2.25 \times 10^{-9} L_{\odot}$, as measured from Cassini data by Li et al., 2012), and $T_{\text{eff}} = 123$ K, close to the values of 124 or 125 K, derived respect-

ively from Voyager 1 (Hanel et al., 2003) and Cassini measurements (Li et al., 2012).

4. Discussion and Conclusions

The formation of a giant planet by core-nucleated accretion requires the growth of a condensed core, several times the Earth's mass, to which gas can bind. This work assumes that the initial reservoir of solids (tens of meters to hundreds of kilometers in size), from which the core grows, is locally available. This assumption implies a high surface density of solids around the formation region. We do not speculate about the origins of these solids. However, if accessible, a sufficiently large concentration of planetesimals can indeed provide an efficient mechanism for planetary growth (see also Voelkel et al., 2020).

The calculations of Paper I showed that a planet's tenuous atmosphere can substantially enhance the accretion of solids during the early stages of the planet's growth (Phase 1; see Figure 5), and an evolving swarm of planetesimals (which accounts for mutual interactions and gas drag, among other effects) contributes to reduce the growth timescale of M_Z until it achieves a few Earth masses (compare models in the left panel of Figure 9). However, once \dot{M}_Z drops below \dot{M}_{XY} and formation enters Phase 2, planet's growth slows down (see again Figure 9). Compared to previous models (e.g., $\sigma 10$ of Movshovitz et al., 2010, which uses the same σ_Z^0 at 5.2 au as assumed here) the core mass is less and the accretion rates of gas and solids are lower, all of which contribute to a lower luminosity. Importantly, the smaller \dot{M}_{XY} indicates that the cooling (i.e., contraction) timescale of the envelope, $\propto M_Z M_{XY} / L$, is longer in the new model. As a result, compared to model $\sigma 10$, Phase 2 lasts much longer: 2 Myr versus 0.5 Myr. It should be noted that the short growth timescale predicted by the old model may actually be difficult to reconcile with the formation of Jupiter, since it would require a relatively massive nebula (a few to several times $0.01 M_\odot$) dispersing in a little over 1 Myr, assuming formation begins early in the evolution of the nebula (see, e.g., Najita and Kenyon, 2014). The present calculations obviate this problem.

Recently, Alibert et al. (2018) presented a scenario for Jupiter's formation based on the accretion of centimeter-size solids followed by the accretion of planetesimals. In their calculations, the planet's mass varies from $5 M_\oplus$ to $16 M_\oplus$ after 1 Myr, a range of values that include the results illustrated in Figure 5.

During Phase 2, M_{XY} increases about linearly in time, at an average rate of $\approx 4.8 \times 10^{-6} M_\oplus \text{ yr}^{-1}$, whereas the heavy-element mass grows on average at $\approx 1.2 \times 10^{-6} M_\oplus \text{ yr}^{-1}$. This result is also similar to the findings of Alibert et al. (2018), who concluded that, between ≈ 1 and ≈ 3 Myr, the planet accreted heavy elements at a rate of order $10^{-6} M_\oplus \text{ yr}^{-1}$. The longest phase of formation is also the faintest (apart from the initial stages of Phase 1, when $M_Z \ll 1 M_\oplus$), see Figure 7, with luminosities hovering just above $10^{-7} L_\odot$, and not exceeding a few times this value. The energy radiated

per unit time is similar to that provided by solids' accretion, Equation (6).

The relatively slow contraction of the envelope affects also the beginning of Phase 3 ($M_{XY} = M_Z$), as the planet takes over 0.8 Myr to double its mass, from 20 to $40 M_\oplus$ (including heavy elements), at an average gas accretion rate of $2 \times 10^{-5} M_\oplus \text{ yr}^{-1}$. This outcome is against the general credence that, past the cross-over mass, the growth timescale of a planet is much shorter than the remainder of the nebula lifetime. However, it helps to reconcile the formation of planets like Saturn, for which gas starvation by gap formation in a protosolar nebula is generally ineffective (Lissauer et al., 2009, and references therein). The outcome is also in accord with the results of Alibert et al. (2018), whose models show that Jupiter attains $M_p \approx 50 M_\oplus$ at around 3 Myr.

The onset of rapid gas accretion ($\dot{M}_{XY} \gg 10^{-3} M_\oplus \text{ yr}^{-1}$) occurs somewhat after $t \approx 3.2$ Myr, when M_p is nearly $60 M_\oplus$. A circumstellar disk of this age around a solar-mass star may sustain an accretion rate (through the disk and on the star) of order $10^{-8} M_\odot \text{ yr}^{-1}$ (Hartmann et al., 2016), and only a fraction is made available to the planet because of disk-planet tidal interactions. From this time onward, the evolution of the planet is tied to that of the surrounding nebula. Simplified accretion disk models, connected to Phases 1, 2, and 3 of the planet's evolution, indicate that the formation of Jupiter can occur within 3.4–4.2 Myr (see Figure 12), in a disk whose initial mass is between 0.05 and $0.1 M_\odot$ (and typical disk's photo-evaporation rates). Depending on the level of kinematic viscosity and disk mass, gas giants can be generated ranging from sub-Saturn to several Jupiter masses, within a few to several Myr (see Figure 11 and Figure 13). For a given disk model, the single largest factor that determines the planet's final mass is likely the duration of Phase 2, which is fairly independent of nebula conditions (provided the disk is not too old when the phase begins).

As the planet evolves along Phase 4, undergoing disk-limited gas accretion, it rapidly contracts as M_p increases. The planet's luminosity rises to values between 10^{-4} and $10^{-3} L_\odot$. Since the planet's mass is $\gtrsim 100 M_\oplus$, and hence its orbit would lie in a tidally-produced gap (in the gaseous disk), these may represent the most favorable conditions to observe a giant planet in formation. The window of opportunity may be short, $\sim 10^5$ years, for more luminous planets, but relatively long, $\sim 10^6$ years, for fainter planets. In these models, Jupiter's effective temperature drops below 1000 K by the end of formation, and the longer the formation time the lower is T_{eff} . It should be emphasized that the power emitted by the planet during the disk-limited accretion phase is primarily that arising from gravitational energy released by the infalling gas, at a surface shock, under the assumption that all energy released there is radiated. The intrinsic luminosity arising from the planet's interior is likely considerably lower (see, e.g., Marley et al., 2007; Mordasini et al., 2012, 2017).

The planet acquires most of its heavy-element content, $M_Z \approx 16 M_\oplus$, prior to the onset of disk-limited accretion, during which time we model the detailed evolution of the planetesimal swarm and the interactions of the solids with

the planet. Of note is that Alibert et al. (2018) also found that up to $20 M_{\oplus}$ worth of heavy elements can be delivered prior to Phase 4. Thereafter, we assume that the planet accretes from the edge of the feeding zone, as this region expands into an undepleted reservoir of solids. Only about $4 M_{\oplus}$ worth of heavy elements are accreted at later stages, a mass determined by the gas-to-solids accretion rates at the beginning of Phase 4 and in agreement with the assessment of Shibata and Ikoma (2019). Although Jupiter could in principle keep accreting planetesimals well after formation, a mechanism is required to deliver solids within a few Hill radii from the planet's orbit. The heavy-element content of the young Jupiter would be consistent with the predictions of Saumon and Guillot (2004) and Militzer et al. (2008), based on interior models of current Jupiter matching gravity data, but it would fall short of other predictions (e.g., Nettelmann et al., 2012; Debras and Chabrier, 2019).

The evolution in isolation of observables such as radius and luminosity (or T_{eff}) soon converges in the three models $\alpha 43$, $\alpha 43\text{LZ}$, and $\alpha 44$, and is basically the same after about 30 Myr. The planet's radius is mostly influenced by the envelope's thermal state, its composition, and equation of state. This is likely the reason that all models, including those presented in Appendix A, result in similar radii at the age of the solar system, exceeding by 6% to 9% Jupiter's present (volumetric mean) radius. The lack of higher abundances of heavy elements in the envelope contributes to the larger value of R_p predicted by these models.

The luminosity of the planet (about 10% in excess of the observed value, see Figure 15) can be affected by the amount of power absorbed from solar radiation. The impact of albedo \mathcal{A} , and quite likely its history, is non-trivial. Estimates of \mathcal{A} were revised upward by using Cassini measurements (see Li et al., 2018) and, as reported in the Appendix, the higher albedo can lower luminosities in the models by 15% at $t = 4567$ Myr. Likewise, a time-varying solar luminosity can impact Jupiter's power output by several percent, at the age of the solar system, as also discussed in the Appendix.

At the current epoch, in Jupiter models $\alpha 43$ and $\alpha 44$, the radius of the heavy-element core is $R_Z \approx 20\,800$ km, about 27% of the planet's radius. This result does not agree with the static (non-evolved) models of the planet that are needed to explain the gravity measurements acquired by the Juno spacecraft. As an example, in a model by Debras and Chabrier (2019) the heavy-element mass fraction X_Z decreases with radius, and is considerably more dilute than in ours, with X_Z decreasing to 10% at 60% of Jupiter's radius. In Wahl et al. (2017), the heavy-element dilute core has a constant X_Z with radius, extending out to about $0.5 R_J$. These interior structures are not consistent with the results of models presented herein, which calculate the full formation and evolution history of the planet. Even if heavy-element deposition in the envelope and the resulting compositional gradients were taken into account, significant discrepancies would likely persist (Lissauer et al., 2020).

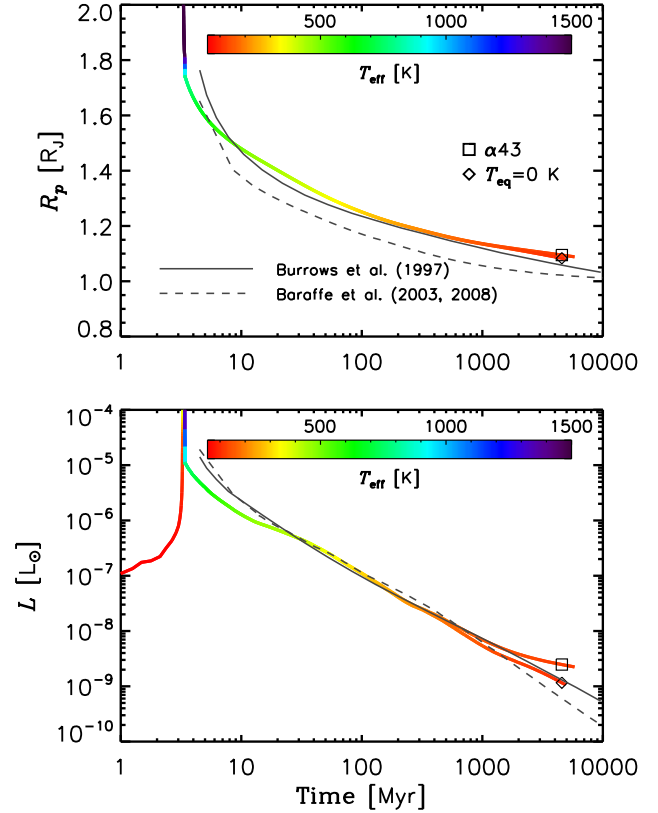


Figure 16: Comparison of the radius (top) and luminosity evolution (bottom) of model $\alpha 43$ and of an analogous model that neglects solar irradiation ($T_{\text{eq}} = 0$ K, see legend in the top panel) against Jupiter's post-formation models of Burrows et al. (1997) and Baraffe et al. (2003, 2008), as indicated, which do not include solar irradiation. Color bars render the planet's effective temperature of the present calculations.

A. Model Comparisons and Refinements

Figure 16 shows the results for the radius (top) and luminosity evolution (bottom) from model $\alpha 43$ and from a version of the same model that does not include solar irradiation (i.e., $T_{\text{eq}} = 0$ K in Equation (14) during the evolution in isolation). The curves are marked, respectively, by a square and a diamond. The figure also shows results from the post-formation calculations of Burrows et al. (1997) and Baraffe et al. (2003, 2008) (see legend in the top panel). These latter models assume non-gray atmospheres, a more sophisticated treatment of radiation transfer compared to the frequency-independent approximation (e.g., Gray, 1992; Mihalas and Weibel Mihalas, 1999) adopted in the calculations presented herein. For purposes of comparison, the evolutionary tracks of Burrows et al. and Baraffe et al. are shifted in time so that they start at the end of Phase 4 of our formation calculation. The case with $T_{\text{eq}} = 0$ K is illustrated because the non-gray atmosphere calculations neglect solar irradiation during evolution. As can be seen in the figure by comparing the irradiated and non-irradiated model, the effects are mostly negligible on R_p , whereas absorption of solar radiation affects the planet's

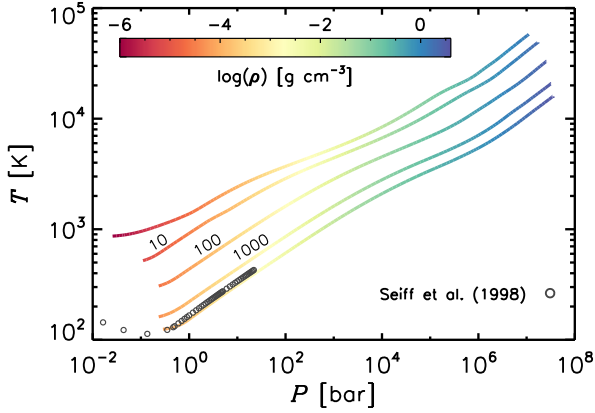


Figure 17: Temperature versus pressure in the planet's envelope at various post-formation epochs, in a variant of model $\alpha 43$ with a compressible core (see text for details on the model). The uppermost curve refers to a time soon after formation ends ($t \approx 3.5$ Myr). Numbers on the three middle curves mark the epochs in Myr. The lowest curve refers to $t = 4.6$ Myr. The open circles represent results from the analysis of Seiff et al. (1998), based on the data acquired by the Galileo entry probe. The curves are color-coded in terms of the gas density at each layer.

power output after several 100 Myr (the difference is less than 10% at $t = 500$ Myr). At the age of the solar system, marked by the symbols, maximum differences in radius between gray and non-gray atmosphere calculations are within 7%. The post-formation luminosity tracks are similar in all models, up to $t \approx 1000$ Myr. They begin to diverge afterward, with the gray atmosphere (non-irradiated) calculation more closely following Burrows et al.'s model.

Temperatures and pressures inside the planet are plotted in Figure 17 at a few epochs after formation, with the top curve indicating a stage right after formation ends (see figure's caption for details). The next three curves beneath represent epochs at 10, 100, and 1000 Myr, respectively, and the last one corresponds to the current age of the planet. The colors render the envelope density in logarithmic scale. Over-plotted to the curves are temperature and pressure data from an analysis by Seiff et al. (1998), which is based on the measurements acquired in 1995 by the Galileo entry probe, during its hour-long descent in Jupiter's atmosphere. The temperature difference at 1 bar is about 8%.

These are results from a version of model $\alpha 43$ that includes a compressible core, as discussed further below. At the core boundary R_Z , the values of density, pressure, and temperature at the current age are $\approx 3.6 \text{ g cm}^{-3}$, $3.5 \times 10^7 \text{ bar}$ (3500 GPa), and $1.6 \times 10^4 \text{ K}$, respectively. For the incompressible-core version of the model ($\alpha 43$), in which R_Z is larger by a factor of about 1.6 at $t \approx 4600$ Myr, these values are instead $\approx 2.7 \text{ g cm}^{-3}$, $2 \times 10^7 \text{ bar}$ (2000 GPa), and $1.3 \times 10^4 \text{ K}$, respectively.

As shown in the bottom panel of Figure 16, solar irradiation can affect Jupiter's luminosity over most of its history. The amount of external radiation absorbed by the planet de-

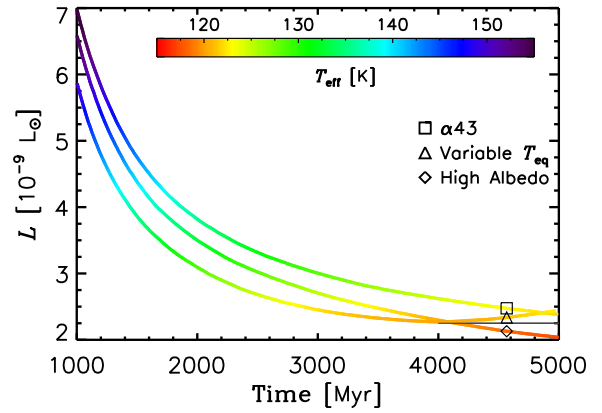


Figure 18: Jupiter's luminosity during isolation for variations of model $\alpha 43$ (curve marked by an open square). The diamond symbol indicates a model in which a higher, constant albedo $\mathcal{A} = 0.503$ is applied to account for absorption from solar irradiation. The triangle indicates a model in which $\mathcal{A} = 0.343$ (as in $\alpha 43$) but the solar luminosity varies according to a stellar model of Spada et al. (2013). The symbols also mark the solar system's age, $t = 4567$ Myr. The color bar renders the planet's effective temperature and the horizontal segment indicates Jupiter's current luminosity.

pends on its albedo, \mathcal{A} . Not only are variations of \mathcal{A} over time unknown, but also its current value has differing estimates. Early Pioneer and Voyager 1 observations resulted in $\mathcal{A} = 0.343$ (Hanel et al., 2003), a value that has been long applied in studies of Jupiter's post-formation evolution (e.g, Fortney and Hubbard, 2003; Mankovich et al., 2016). However, an analysis of Cassini multi-instrument observations (Li et al., 2018) provided a higher estimate of Jupiter's albedo, $\mathcal{A} = 0.503$, which would reduce the equilibrium temperature to $T_{\text{eq}} \approx 102.7 \text{ K}$. A calculation of model $\alpha 43$, applying this lower equilibrium temperature, results in a planet radius only marginally different from that illustrated in Figure 15 (at $t = 4567$ Myr), whereas the effect on the luminosity is larger, as shown in Figure 18 (see curve marked by a diamond), bringing L within 5% of the observed value.

The Sun's luminosity has changed over the age of the solar system. In order to gauge the effect of the varying solar power output on Jupiter's luminosity, a calculation of model $\alpha 43$ is performed by using a time-dependent solar luminosity from a solar-type stellar model of Spada et al. (2013). Results are illustrated in Figure 18. The luminosity, marked by a triangle in the figure, is lower than in model $\alpha 43$ over most of the planet's history but it becomes larger after 4800 Myr. The planet radius in the three models in the figure is largely unaffected and, at the age of the solar system, is the same within 1%.

As mentioned in Section 2.1, the calculations assume that accreted solids sediment to the center, eventually accumulating on an incompressible core of heavy elements. But self-gravity and pressure exerted by the overlying gaseous envelope can compress the core. To relax this approximation, structure models of the core are calculated according

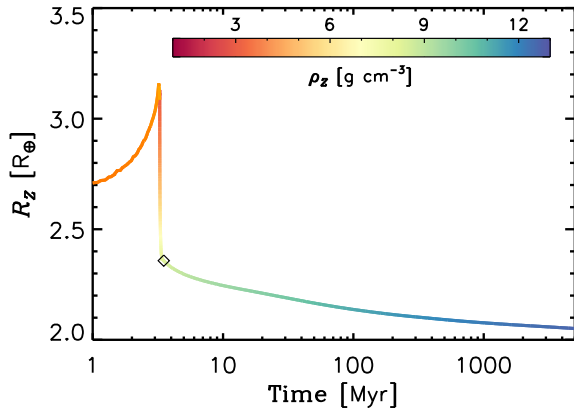


Figure 19: Radius of the ice and silicate core versus time in a version of model $\alpha 43$ in which compression of the heavy elements is taken into account as described in the text. The curve is color-coded according to the core's mean density (mass-to-volume ratio). The heavy-element composition is the same as that of the accreted solids, H_2O and silicates in a ratio 58/42 by mass. The diamond symbol indicates the end of Phase 4 and beginning of isolation.

to the procedure described in D'Angelo and Bodenheimer (2016). The core is assumed to be in hydrostatic equilibrium and to have a fully adiabatic interior, a good approximation given the relatively high interior temperatures (we are mostly concerned with late Phase 2 and beyond). The composition is that of accreted solids, ice and silicates in a mass ratio of 58/42. Given M_Z , and temperature and pressure at the base of the envelope, the core radius R_Z is provided by interpolation of values from a dense table based on these structure models.

Figure 19 illustrates results from a calculation of a version of model $\alpha 43$ that accounts for a compressible core. The radius R_Z is plotted as a function of time and the diamond symbol on the curve marks the end of formation. The curve is color-coded according to the core's mean density, ρ_Z . The radius R_Z increases, as M_Z grows, up to a maximum of a little over $3.1 R_\oplus$, when $M_Z \approx 15 M_\oplus$. This happens in Phase 3, before rapid contraction begins. From this point, and until the end of formation, the pressure exerted at the base of the envelope increases by a factor of 25, from ≈ 44 to 1110 GPa. Although the temperature at R_Z rises from $\approx 2 \times 10^4$ to $\approx 5.8 \times 10^4$ K and M_Z grows, the core shrinks by about 25%, to $2.37 R_\oplus$. At the end of formation, differences in planet radius are marginal (a few percent), whereas the luminosity is lower than in model $\alpha 43$, by about 35%. Contraction of the core continues during the isolation phase, as the envelope cools and the pressure exerted on it increases. At $t = 4567$ Myr, $R_Z \approx 2.05 R_\oplus$ and both $L = 2.44 \times 10^{-9} L_\odot$ and $R_p = 1.06 R_J$ are within a few percent of the values obtained from model $\alpha 43$.

Acknowledgements

We wish to thank two anonymous reviewers whose comments helped improve this manuscript. Primary support for this research was provided by NASA's Emerging Worlds program (proposals 80HQTR19T0071, 18-EW18_2-0060, and 15-EW15_2-0007). Additional support was provided by NASA's Exoplanets Research Program (proposal 18-XRP18_2-0106) and through NASA grant NNX14AG92G. Computational resources supporting this work were provided by the NASA High-End Computing (HEC) Program through the NASA Advanced Supercomputing (NAS) Division at Ames Research Center.

References

- Adachi, I., Hayashi, C., Nakazawa, K., 1976. The Gas Drag Effect on the Elliptical Motion of a Solid Body in the Primordial Solar Nebula. *Progress of Theoretical Physics* 56, 1756–1771.
- Alibert, Y., Venturini, J., Helled, R., Ataiee, S., Burn, R., Senecal, L., Benz, W., Mayer, L., Mordasini, C., Quanz, S.P., Schönbachler, M., 2018. The formation of Jupiter by hybrid pebble-planetesimal accretion. *Nature Astronomy* 2, 873–877. doi:10.1038/s41550-018-0557-2, arXiv:1809.05383.
- Archinal, B.A., A'Hearn, M.F., Bowell, E., Conrad, A., Consolmagno, G.J., Courtin, R., Fukushima, T., Hestroffer, D., Hilton, J.L., Krasinsky, G.A., Neumann, G., Oberst, J., Seidelmann, P.K., Stooke, P., Tholen, D.J., Thomas, P.C., Williams, I.P., 2011. Report of the iau working group on cartographic coordinates and rotational elements: 2009. *Celestial Mechanics and Dynamical Astronomy* 109, 101–135. URL: <https://doi.org/10.1007/s10569-010-9320-4>, doi:10.1007/s10569-010-9320-4.
- Armitage, P.J., 2020. *Protoplanetary Disk Evolution*. 2 ed.. Cambridge University Press. pp. 86–140. doi:10.1017/9781108344227.004.
- Asplund, M., Grevesse, N., Sauval, A.J., Scott, P., 2009. The Chemical Composition of the Sun. *ARA&A* 47, 481–522. doi:10.1146/annurev.astro.46.060407.145222, arXiv:0909.0948.
- Baraffe, I., Chabrier, G., Barman, T., 2008. Structure and evolution of super-Earth to super-Jupiter exoplanets. I. Heavy element enrichment in the interior. *A&A* 482, 315–332. doi:10.1051/0004-6361:20079321, arXiv:0802.1810.
- Baraffe, I., Chabrier, G., Barman, T.S., Allard, F., Hauschildt, P.H., 2003. Evolutionary models for cool brown dwarfs and extrasolar giant planets. The case of HD 209458. *A&A* 402, 701–712. doi:10.1051/0004-6361:20030252, arXiv:astro-ph/0302293.
- Bodenheimer, P., D'Angelo, G., Lissauer, J.J., Fortney, J.J., Saumon, D., 2013. Deuterium Burning in Massive Giant Planets and Low-Mass Brown Dwarfs formed by Core-Nucleated Accretion. *ApJ* 770, 120. doi:10.1088/0004-637x/770/2/120.
- Bodenheimer, P., Hubickyj, O., Lissauer, J.J., 2000. Models of the in situ formation of detected extrasolar giant planets. *Icarus* 143, 2–14. doi:10.1006/icar.1999.6246.
- Bodenheimer, P., Stevenson, D.J., Lissauer, J.J., D'Angelo, G., 2018. New Formation Models for the Kepler-36 System. *ApJ* 868, 138. doi:10.3847/1538-4357/aae928, arXiv:1810.07160.
- Burrows, A., Marley, M., Hubbard, W.B., Lunine, J.I., Guillot, T., Saumon, D., Freedman, R., Sudarsky, D., Sharp, C., 1997. A Nongray Theory of Extrasolar Giant Planets and Brown Dwarfs. *ApJ* 491, 856–875. doi:10.1086/305002, arXiv:astro-ph/9705201.
- Chambers, J.E., O'Brien, D.P., Davis, A.M., 2010. Accretion of Planetesimals and the Formation of Rocky Planets. *Protoplanetary Dust: Astrophysical and Cosmochemical Perspectives*, edited by Apai, D. A. and Lauretta, D. S. Cambridge, UK: Cambridge University Press. pp. 299–335.
- Chiang, E., Youdin, A.N., 2010. Forming Planetesimals in Solar and Extrasolar Nebulae. *Annual Review of Earth and Planetary Sciences* 38, 493–522. doi:10.1146/annurev-earth-040809-152513, arXiv:0909.2652.
- Connelly, J.N., Bizzarro, M., Krot, A.N., Nordlund, Å., Wielandt, D., Ivanova, M.A., 2012. The Absolute Chronology and Thermal Pro-

- cessing of Solids in the Solar Protoplanetary Disk. *Science* 338, 651. doi:10.1126/science.1226919.
- D'Angelo, G., Bodenheimer, P., 2013. Three-dimensional Radiation-hydrodynamics Calculations of the Envelopes of Young Planets Embedded in Protoplanetary Disks. *ApJ* 778, 77. doi:10.1088/0004-637X/778/1/77, arXiv:1310.2211.
- D'Angelo, G., Bodenheimer, P., 2016. In Situ and Ex Situ Formation Models of Kepler 11 Planets. *ApJ* 828, 33. doi:10.3847/0004-637X/828/1/33, arXiv:1606.08088.
- D'Angelo, G., Lubow, S.H., 2008. Evolution of Migrating Planets Undergoing Gas Accretion. *ApJ* 685, 560–583. doi:10.1086/590904, arXiv:0806.1771.
- D'Angelo, G., Podolak, M., 2015. Capture and Evolution of Planetesimals in Circumjovian Disks. *ApJ* 806, 203. doi:10.1088/0004-637X/806/2/203, arXiv:1504.04364.
- D'Angelo, G., Weidenschilling, S.J., Lissauer, J.J., Bodenheimer, P., 2014. Growth of Jupiter: Enhancement of core accretion by a voluminous low-mass envelope. *Icarus* 241, 298–312. doi:10.1016/j.icarus.2014.06.029, arXiv:1405.7305.
- Debras, F., Chabrier, G., 2019. New models of jupiter in the context of Juno and Galileo. *ApJ* 872, 100. URL: <https://doi.org/10.3847/2F1538-4357%2Faaff65>, doi:10.3847/1538-4357/aaff65.
- Eggleton, P.P., 1983. Approximations to the radii of Roche lobes. *ApJ* 268, 368–369. doi:10.1086/160960.
- Ercolano, B., Pascucci, I., 2017. The dispersal of planet-forming discs: theory confronts observations. *Royal Society Open Science* 4, 170114. doi:10.1098/rsos.170114, arXiv:1704.00214.
- Fortney, J.J., Hubbard, W.B., 2003. Phase separation in giant planets: inhomogeneous evolution of Saturn. *Icarus* 164, 228 – 243. URL: <http://www.sciencedirect.com/science/article/pii/S0019103503001301>, doi:https://doi.org/10.1016/S0019-1035(03)00130-1.
- Gorti, U., Hollenbach, D., Dullemond, C.P., 2015. The Impact of Dust Evolution and Photoevaporation on Disk Dispersal. *ApJ* 804, 29. doi:10.1088/0004-637X/804/1/29, arXiv:1502.07369.
- Gorti, U., Liseau, R., Sándor, Z., Clarke, C., 2016. Disk Dispersal: Theoretical Understanding and Observational Constraints. *Space Sci. Rev.* 205, 125–152. doi:10.1007/s11214-015-0228-x, arXiv:1512.04622.
- Gray, D.F., 1992. *The Observation and Analysis of Stellar Photospheres*. Cambridge, UK: Cambridge University Press.
- Greenberg, R., 1983. The role of dissipation in shepherding of ring particles. *Icarus* 53, 207–218. doi:10.1016/0019-1035(83)90142-2.
- Greenzweig, Y., Lissauer, J.J., 1992. Accretion rates of protoplanets. II - Gaussian distributions of planetesimal velocities. *Icarus* 100, 440–463. doi:10.1016/0019-1035(92)90110-5.
- Hanel, R.A., Conrath, B.J., Jennings, D.E., Samuelson, R.E., 2003. Interpretation of results. 2 ed.. *Exploration of the Solar System by Infrared Remote Sensing*. Cambridge, UK: Cambridge University Press. pp. 405–464. doi:10.1017/CB09780511536106.011.
- Hartmann, L., Herczeg, G., Calvet, N., 2016. Accretion onto pre-main-sequence stars. *Annual Review of Astronomy and Astrophysics* 54, 135–180. URL: <https://doi.org/10.1146/annurev-astro-081915-023347>, doi:10.1146/annurev-astro-081915-023347, arXiv:https://doi.org/10.1146/annurev-astro-081915-023347.
- Hubickyj, O., Bodenheimer, P., Lissauer, J.J., 2005. Accretion of the gaseous envelope of Jupiter around a 5–10 Earth-mass core. *Icarus* 179, 415–431. doi:10.1016/j.icarus.2005.06.021.
- Kary, D.M., Lissauer, J.J., 1994. Numerical simulations of planetary growth. *Numerical Simulations in Astrophysics*, edited by Franco, J., Lizano, S., Aguilar, L., and Daltabuit, E. Cambridge, UK: Cambridge University Press. p. 364.
- Kary, D.M., Lissauer, J.J., 1995. Nebular gas drag and planetary accretion. II. Planet on an eccentric orbit. *Icarus* 117, 1–24. doi:10.1006/icar.1995.1139.
- Kary, D.M., Lissauer, J.J., Greenzweig, Y., 1993. Nebular Gas Drag and Planetary Accretion. *Icarus* 106, 288–307. doi:10.1006/icar.1993.1172.
- Kippenhahn, R., Weigert, A., Weiss, A., 2013. *Stellar Structure and Evolution*. Astronomy and Astrophysics Library, ISBN 978-3-642-30255-8. Springer-Verlag Berlin Heidelberg, 2013. doi:10.1007/978-3-642-30304-3.
- Levison, H.F., Thommes, E., Duncan, M.J., 2010. Modeling the Formation of Giant Planet Cores. I. Evaluating Key Processes. *AJ* 139, 1297–1314. doi:10.1088/0004-6256/139/4/1297, arXiv:0912.3144.
- Li, L., Baines, K.H., Smith, M.A., West, R.A., Pérez-Hoyos, S., Trammell, H.J., Simon-Miller, A.A., Conrath, B.J., Gierasch, P.J., Orton, G.S., Nixon, C.A., Filacchione, G., Fry, P.M., Mormary, T.W., 2012. Emitted power of Jupiter based on Cassini CIRS and Vims observations. *Journal of Geophysical Research: Planets* 117, E11002. URL: <https://agupubs.onlinelibrary.wiley.com/doi/abs/10.1029/2012JE004191>, doi:10.1029/2012JE004191, arXiv:https://agupubs.onlinelibrary.wiley.com/doi/pdf/10.1029/2012JE004191.
- Li, L., Jiang, X., West, R.A., Gierasch, P.J., Perez-Hoyos, S., Sanchez-Lavega, A., Fletcher, L.N., Fortney, J.J., Knowles, B., Porco, C.C., Baines, K.H., Fry, P.M., Mallama, A., Achterberg, R.K., Simon, A.A., Nixon, C.A., Orton, G.S., Dyudina, U.A., Ewald, S.P., Schumde, R.W., 2018. Less absorbed solar energy and more internal heat for Jupiter. *Nature Communications* 9, 3709. doi:10.1038/s41467-018-06107-2.
- Lissauer, J.J., 1987. Timescales for Planetary Accretion and the Structure of the Protoplanetary Disk. *Icarus* 69, 249–265. doi:10.1016/0019-1035(87)90104-7.
- Lissauer, J.J., Bodenheimer, P., Stevenson, D.J., D'Angelo, G., 2020. Mixing of Condensable Constituents with H/He During Formation of Jupiter, in: *American Astronomical Society Meeting Abstracts*, p. 221.01.
- Lissauer, J.J., Hubickyj, O., D'Angelo, G., Bodenheimer, P., 2009. Models of Jupiter's growth incorporating thermal and hydrodynamic constraints. *Icarus* 199, 338–350. doi:10.1016/j.icarus.2008.10.004, arXiv:0810.5186.
- Lubow, S.H., Ida, S., 2010. *Planet Migration. Exoplanets*, edited by S. Seager. Tucson, AZ: University of Arizona Press. pp. 347–371.
- Lynden-Bell, D., Pringle, J.E., 1974. The evolution of viscous discs and the origin of the nebular variables. *MNRAS* 168, 603–637. doi:10.1093/mnras/168.3.603.
- Mankovich, C., Fortney, J.J., Moore, K.L., 2016. Bayesian Evolution Models for Jupiter with Helium Rain and Double-diffusive Convection. *ApJ* 832, 113. doi:10.3847/0004-637X/832/2/113, arXiv:1609.09070.
- Marley, M.S., Fortney, J.J., Hubickyj, O., Bodenheimer, P., Lissauer, J.J., 2007. On the luminosity of young Jupiters. *ApJ* 655, 541–549. doi:10.1086/509759, arXiv:arXiv:astro-ph/0609739.
- Mihalas, D., Weibel Mihalas, B., 1999. *Foundations of radiation hydrodynamics*. New York: Dover, 1999.
- Militzer, B., Hubbard, W.B., Vorberger, J., Tamblyn, I., Bonev, S.A., 2008. A Massive Core in Jupiter Predicted from First-Principles Simulations. *ApJ* 688, L45–L48. doi:10.1086/594364, arXiv:0807.4264.
- Morbidelli, A., Levison, H.F., Tsiganis, K., Gomes, R., 2005. Chaotic capture of Jupiter's Trojan asteroids in the early Solar System. *Nature* 435, 462–465. doi:10.1038/nature03540.
- Mordasini, C., Alibert, Y., Klahr, H., Henning, T., 2012. Characterization of exoplanets from their formation. I. Models of combined planet formation and evolution. *A&A* 547, A111. doi:10.1051/0004-6361/201118457, arXiv:1206.6103.
- Mordasini, C., Marleau, G.D., Mollière, P., 2017. Characterization of exoplanets from their formation. III. The statistics of planetary luminosities. *A&A* 608, A72. doi:10.1051/0004-6361/201630077, arXiv:1708.00868.
- Movshovitz, N., Bodenheimer, P., Podolak, M., Lissauer, J.J., 2010. Formation of Jupiter using opacities based on detailed grain physics. *Icarus* 209, 616–624. doi:10.1016/j.icarus.2010.06.009, arXiv:1005.3875.
- Najita, J.R., Kenyon, S.J., 2014. The mass budget of planet-forming discs: isolating the epoch of planetesimal formation. *MNRAS* 445, 3315–3329. doi:10.1093/mnras/stu1994, arXiv:1409.7021.
- Natta, A., Testi, L., Randich, S., 2006. Accretion in the ρ -Ophiuchi pre-main sequence stars. *A&A* 452, 245–252. doi:10.1051/0004-6361:20054706, arXiv:astro-ph/0602618.
- Nelson, R.P., 2018. *Planetary Migration in Protoplanetary Disks*. Springer International Publishing, Cham. pp. 2287–2317. URL: https://doi.org/10.1007/978-3-319-55333-7_139, doi:10.1007/978-3-319-55333-7_139.
- Nesvorný, D., Vokrouhlický, D., Morbidelli, A., 2013. Capture of Trojans by Jumping Jupiter. *ApJ* 768, 45. doi:10.1088/0004-637X/768/1/45,

- arXiv:1303.2900.
- Nettelmann, N., Becker, A., Holst, B., Redmer, R., 2012. Jupiter Models with Improved Ab Initio Hydrogen Equation of State (H-REOS.2). *ApJ* 750, 52. doi:10.1088/0004-637X/750/1/52, arXiv:1109.5644.
- Picogna, G., Ercolano, B., Owen, J.E., Weber, M.L., 2019. The dispersal of protoplanetary discs - I. A new generation of X-ray photo-evaporation models. *MNRAS* 487, 691–701. doi:10.1093/mnras/stz1166, arXiv:1904.02752.
- Podolak, M., Pollack, J.B., Reynolds, R.T., 1988. Interactions of planetesimals with protoplanetary atmospheres. *Icarus* 73, 163–179. doi:10.1016/0019-1035(88)90090-5.
- Pollack, J.B., Hollenbach, D., Beckwith, S., Simonelli, D.P., Roush, T., Fong, W., 1994. Composition and radiative properties of grains in molecular clouds and accretion disks. *ApJ* 421, 615–639. doi:10.1086/173677.
- Pollack, J.B., Hubickyj, O., Bodenheimer, P., Lissauer, J.J., Podolak, M., Greenzweig, Y., 1996. Formation of the giant planets by concurrent accretion of solids and gas. *Icarus* 124, 62–85. doi:10.1006/icar.1996.0190.
- Pringle, J.E., 1981. Accretion discs in astrophysics. *ARA&A* 19, 137–162. doi:10.1146/annurev.aa.19.090181.001033.
- Ribas, I., 2010. The Sun and stars as the primary energy input in planetary atmospheres, in: Kosovichev, A.G., Andrei, A.H., Rozelot, J.P. (Eds.), *Solar and Stellar Variability: Impact on Earth and Planets*, pp. 3–18. doi:10.1017/S1743921309992298, arXiv:0911.4872.
- Saumon, D., Guillot, T., 2004. Shock Compression of Deuterium and the Interiors of Jupiter and Saturn. *ApJ* 609, 1170–1180. doi:10.1086/421257, arXiv:arXiv:astro-ph/0403393.
- Seiff, A., Kirk, D.B., Knight, T.C.D., Young, R.E., Mihalov, J.D., Young, L.A., Milos, F.S., Schubert, G., Blanchard, R.C., Atkinson, D., 1998. Thermal structure of jupiter's atmosphere near the edge of a 5- μ m hot spot in the north equatorial belt. *Journal of Geophysical Research: Planets* 103, 22857–22889. URL: <https://agupubs.onlinelibrary.wiley.com/doi/abs/10.1029/98JE01766>, doi:10.1029/98JE01766, arXiv:https://agupubs.onlinelibrary.wiley.com/doi/pdf/10.1029/98JE01766.
- Shakura, N.I., Sunyaev, R.A., 1973. Black holes in binary systems. Observational appearance. *A&A* 24, 337–355.
- Shibata, S., Ikoma, M., 2019. Capture of solids by growing proto-gas giants: effects of gap formation and supply limited growth. *MNRAS* 487, 4510–4524. doi:10.1093/mnras/stz1629, arXiv:1906.05530.
- Slyusarev, I.G., Belskaya, I.N., 2014. Jupiter's trojans: Physical properties and origin. *Solar System Research* 48, 139–157. URL: <https://doi.org/10.1134/S0038094614020063>, doi:10.1134/S0038094614020063.
- Spada, F., Demarque, P., Kim, Y.C., Sills, A., 2013. The Radius Discrepancy in Low-mass Stars: Single versus Binaries. *ApJ* 776, 87. doi:10.1088/0004-637X/776/2/87, arXiv:1308.5558.
- Voelkel, O., Klahr, H., Mordasini, C., Emsenhuber, A., Lenz, C., 2020. Effect of pebble flux-regulated planetesimal formation on giant planet formation. *A&A in press*. doi:10.1051/0004-6361/202038085.
- Wahl, S.M., Hubbard, W.B., Militzer, B., Guillot, T., Miguel, Y., Movshovitz, N., Kaspi, Y., Helled, R., Reese, D., Galanti, E., Levin, S., Connerney, J.E., Bolton, S.J., 2017. Comparing Jupiter interior structure models to Juno gravity measurements and the role of a dilute core. *Geophys. Res. Lett.* 44, 4649–4659. doi:10.1002/2017GL073160, arXiv:1707.01997.
- Ward, W.R., 1997. Protoplanet Migration by Nebula Tides. *Icarus* 126, 261–281. doi:10.1006/icar.1996.5647.
- Weidenschilling, S.J., 1977. Aerodynamics of solid bodies in the solar nebula. *MNRAS* 180, 57–70. doi:10.1093/mnras/180.1.57.
- Weidenschilling, S.J., 2005. Formation of the Cores of the Outer Planets. *Space Science Reviews* 116, 53–66. doi:10.1007/s11214-005-1947-1.
- Weidenschilling, S.J., 2011. Initial sizes of planetesimals and accretion of the asteroids. *Icarus* 214, 671–684. doi:10.1016/j.icarus.2011.05.024.
- Weidenschilling, S.J., Spaute, D., Davis, D.R., Marzari, F., Ohtsuki, K., 1997. Accretional Evolution of a Planetesimal Swarm. *Icarus* 128, 429–455. doi:10.1006/icar.1997.5747.
- Weiss, A., Hillebrandt, W., Thomas, H.C., Ritter, H., 2006. *Cox and Giuli's Principles of Stellar Structure*. Cambridge, UK: Cambridge Scientific Publishers Ltd, 2006.